RESEARCH ARTICLE

PRC2-Inactivating Mutations in Cancer Enhance Cytotoxic Response to DNMT1-Targeted Therapy via Enhanced Viral Mimicry

Amish J. Patel[1], Sarah Warda[1], Jesper L.V. Maag[2], Rohan Misra[3], Miguel A. Miranda-Román[1,4], Mohini R. Pachai[1], Cindy J. Lee[1], Dan Li[1], Naitao Wang[1], Gabriella Bayshtok[1], Eve Fishinevich[1], Yinuo Meng[5], Elissa W.P. Wong[1], Juan Yan[1], Emily Giff[1], Melissa B. Pappalardi[6], Michael T. McCabe[6], Jonathan A. Fletcher[7], Charles M. Rudin[8,9], Sarat Chandarlapaty[1,10,11], Joseph M. Scandura[12,13,14], Richard P. Koche[2], Jacob L. Glass[1,2,15], Cristina R. Antonescu[16], Deyou Zheng[17,18,19], Yu Chen[1,4,5,20,21], and Ping Chi[1,4,5,20,21]

ABSTRACT Polycomb repressive complex 2 (PRC2) has oncogenic and tumor-suppressive roles in cancer. There is clinical success of targeting this complex in PRC2-dependent cancers, but an unmet therapeutic need exists in PRC2-loss cancer. PRC2-inactivating mutations are a hallmark feature of high-grade malignant peripheral nerve sheath tumor (MPNST), an aggressive sarcoma with poor prognosis and no effective targeted therapy. Through RNAi screening in MPNST, we found that PRC2 inactivation increases sensitivity to genetic or small-molecule inhibition of DNA methyltransferase 1 (DNMT1), which results in enhanced cytotoxicity and antitumor response. Mechanistically, PRC2 inactivation amplifies DNMT inhibitor–mediated expression of retrotransposons, subsequent viral mimicry response, and robust cell death in part through a protein kinase R (PKR)–dependent double-stranded RNA sensor. Collectively, our observations posit DNA methylation as a safeguard against antitumorigenic cell-fate decisions in PRC2-loss cancer to promote cancer pathogenesis, which can be therapeutically exploited by DNMT1-targeted therapy.

SIGNIFICANCE: PRC2 inactivation drives oncogenesis in various cancers, but therapeutically targeting PRC2 loss has remained challenging. Here we show that PRC2-inactivating mutations set up a tumor context–specific liability for therapeutic intervention via DNMT1 inhibitors, which leads to innate immune signaling mediated by sensing of derepressed retrotransposons and accompanied by enhanced cytotoxicity.

See related commentary by Guil and Esteller, p. 2020.

[1]Human Oncology and Pathogenesis Program, Memorial Sloan Kettering Cancer Center, New York, New York. [2]Center for Epigenetics Research, Memorial Sloan Kettering Cancer Center, New York, New York. [3]Department of Genetics, Albert Einstein College of Medicine, Bronx, New York. [4]Louis V. Gerstner, Jr. Graduate School of Biomedical Sciences, Memorial Sloan Kettering Cancer Center, New York, New York. [5]Weill Cornell Graduate School of Medical Sciences, Cornell University, New York, New York. [6]Cancer Epigenetics Research Unit, Oncology, GlaxoSmithKline, Collegeville, Pennsylvania. [7]Department of Pathology, Brigham and Women's Hospital, Harvard Medical School, Boston, Massachusetts. [8]Department of Medicine, Thoracic Oncology Service, Memorial Sloan Kettering Cancer Center, New York, New York. [9]Molecular Pharmacology Program, Memorial Sloan Kettering Cancer Center, New York, New York. [10]Breast Medicine Service, Department of Medicine, Memorial Sloan Kettering Cancer Center, New York, New York. [11]Weill Cornell Medical College, New York, New York. [12]Laboratory of Molecular Hematopoiesis, Hematology and Oncology, Weill Cornell Medicine, New York, New York. [13]Richard T. Silver MD Myeloproliferative Neoplasm Center, Weill Cornell Medicine, New York, New York. [14]Regenerative Medicine, Department of Medicine, Weill Cornell Medicine, New York, New York. [15]Leukemia Service, Memorial Sloan Kettering Cancer Center, New York, New York. [16]Department of Pathology, Memorial Sloan Kettering Cancer Center, New York, New York. [17]The Saul R. Korey Department of Neurology, Albert Einstein College of Medicine, Bronx, New York. [18]Department of Genetics, Albert Einstein College of Medicine, Bronx, New York. [19]Dominick P. Purpura Department of Neuroscience, Albert Einstein College of Medicine, Bronx, New York. [20]Department of Medicine, Memorial Sloan Kettering Cancer Center, New York, New York. [21]Department of Medicine, Weill Cornell Medical College, New York, New York.

Corresponding Authors: Yu Chen, Memorial Sloan Kettering Cancer Center, 1275 York Avenue, New York, NY 10065. Phone: 646-888-3356; E-mail: cheny1@mskcc.org; and Ping Chi, Memorial Sloan Kettering Cancer Center, 1275 York Avenue, New York, NY 10065. Phone: 646-888-3338; E-mail: chip@mskcc.org

Cancer Discov 2022;12:2120–39

doi: 10.1158/2159-8290.CD-21-1671

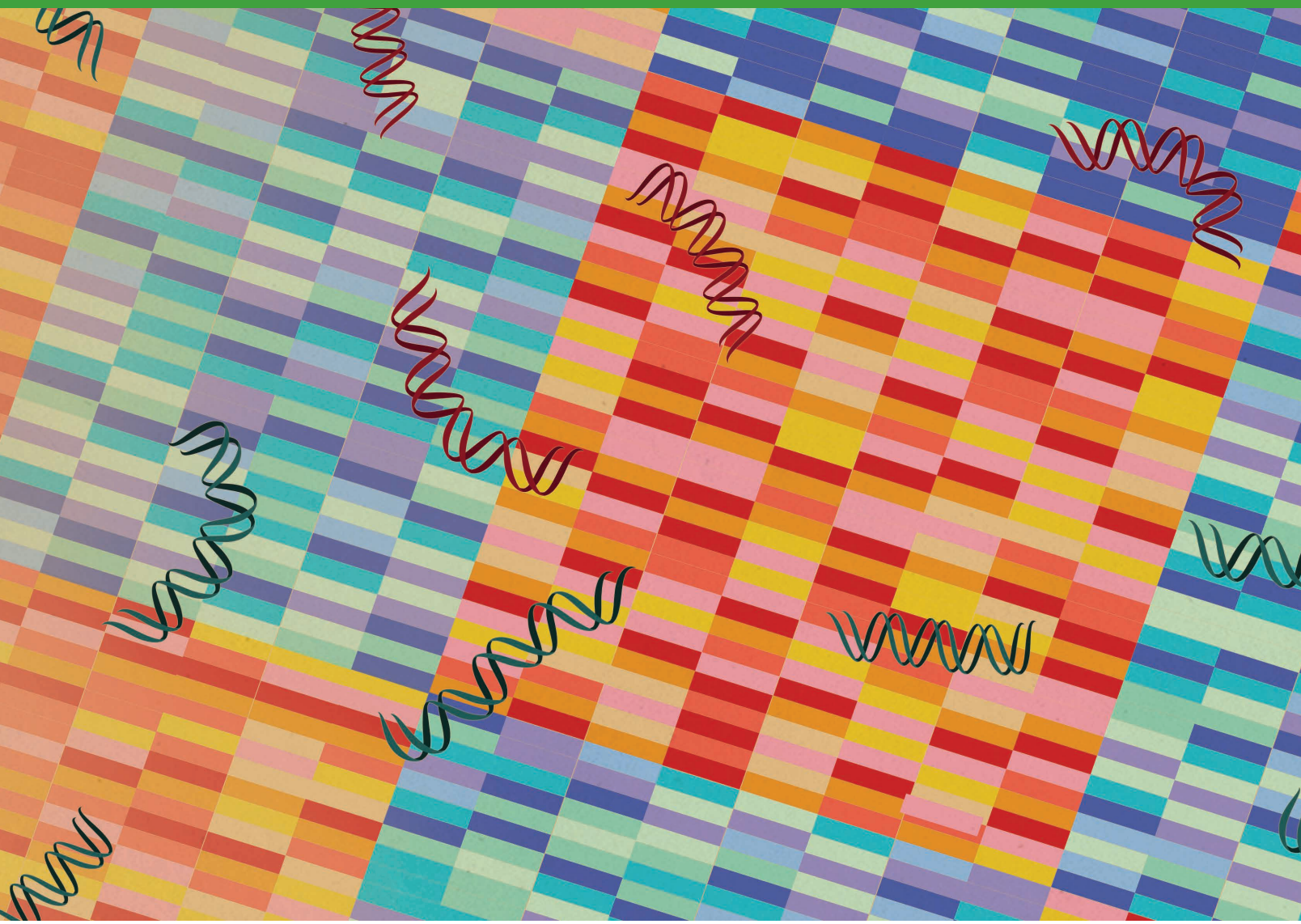

INTRODUCTION

The PRC2 complex consisting of core components SUZ12, EED, and EZH1/2 establishes and maintains H3K27me2/3 throughout the genome and regulates chromatin structure, transcription, cellular stemness, and differentiation (1). In cancer pathogenesis, PRC2 can function as an oncogenic driver through *EZH2* overexpression in various cancers (2, 3) and gain-of-function *EZH2* mutations in lymphomas (4); PRC2 can also function as a tumor suppressor through inactivating genetic alterations in myeloid disorders (5, 6), T-cell acute lymphoblastic leukemia (ALL; ref. 7), early T-cell precursor ALL (8), melanoma (9), and malignant peripheral nerve sheath tumor (MPNST; refs. 9–11) or by functional inactivation via oncohistone mutations (H3K27M) in pediatric gliomas (12). Complete inactivation of PRC2 is most prevalent, occurring in ~80% of high-grade MPNSTs (13).

MPNST represents an aggressive subtype of soft-tissue sarcoma with a poor prognosis due to the surgical challenges in local control and lack of effective systemic therapy. They occur in distinct clinical settings—type I neurofibromatosis (NF1)–associated (45%), sporadic (45%), or radiation (RT)-associated (10%)—but share highly recurrent and biallelic genetic inactivation of three tumor suppressor pathways: *NF1*, *CDKN2A*, and PRC2 (*EED* or *SUZ12*; refs. 9, 10, 11). PRC2 inactivation results in a global loss of H3K27me2/3 and aberrant transcriptional activation of developmentally silenced master regulators, leading to enhanced cellular plasticity in MPNST (10, 13, 14). Therapeutically targeting PRC2 inactivation in cancer remains a challenge and requires relevant context-specific cancer models for therapeutic discovery and development.

To discover vulnerabilities specified or enhanced by PRC2-inactivating alterations in their relevant cancer setting, we conducted an epigenome-focused pooled RNAi dropout screen in patient-derived MPNST cell lines. We identified and validated DNMT1, whose downregulation resulted in enhanced growth inhibition in PRC2-loss MPNST *in vitro* and *in vivo*. Therapeutic targeting of DNMT1 with the FDA-approved decitabine [DAC; a pan-DNMT inhibitor (DNMTi)]

or a novel preclinical DNMT1-selective catalytic inhibitor led to significantly enhanced cytotoxicity dependent on the loss of PRC2 enzymatic activity. Mechanistically, PRC2 and DNA methylation coregulate transcriptional silencing of a subset of H3K27me3-enriched transcriptional targets and retrotransposons. Loss of PRC2 function amplifies DNMTi therapy–induced transcriptional activation of retrotransposons and subsequent viral mimicry–mediated cell death through the double-stranded RNA (dsRNA) sensor protein kinase R (PKR). These data point to PRC2-inactivating mutations as drivers of cancer pathogenesis and liabilities that prime for tumor cell–selective and robust cell death via DNMT1-targeted therapy while sparing PRC2 wild-type (WT) normal cells.

RESULTS

RNAi Screening Identifies *DNMT1* Synthetic Lethality with PRC2 Inactivation in Cancer

To identify epigenetic factors that pose selective synthetic lethal interactions with PRC2 inactivation, we conducted a pooled doxycycline-inducible short hairpin RNA (shRNA) screen targeting 565 known epigenetic/chromatin regulators in PRC2-WT and PRC2-loss patient-derived MPNST cell lines. We authenticated that all cell lines had complete loss of both *NF1* and *CDKN2A*, and five of seven (~71%) cell lines had complete PRC2 inactivation by Memorial Sloan Kettering-Integrated Mutation Profiling of Actional Cancer Targets (MSK-IMPACT; ref. 15) and/or immunoblotting (Fig. 1A; Supplementary Fig. S1A). After shRNA screening (Fig. 1B), we used HiTSelect (16) to rank each set of five shRNAs per gene in the library across all cell lines in the screen for depletion (negative selection; Supplementary Table S1). As anticipated, shRNAs targeting an essential gene (e.g., *ACTB*) were ranked among the top (most significant), whereas nontoxic control shRNA (sh*Ren*.713) was ranked at the bottom (least significant) across all cell lines (Fig. 1C). Among all candidates, *DNMT1*-specific shRNAs were ranked consistently among the top 10 statistically significant candidates for negative selection across all PRC2-loss but not PRC2-WT cell lines (Fig. 1C). *DNMT1* encodes a DNA methyltransferase responsible for maintaining DNA methylation (5-methylcytosine) at CpG dinucleotides on newly replicated DNA during cellular division (17). Interestingly, shRNAs specific for *de novo* DNA methyltransferases (*DNMT3A* and *DNMT3B*) were less significantly ranked in the screen (Fig. 1C). *DNMT1*, *DNMT3A*, and *DNMT3B* are rarely mutated in patient-derived human MPNST cell lines and tumors (Supplementary Fig. S1A and S1B). Moreover, *DNMT1* is consistently and abundantly expressed in all human MPNST cell lines irrespective of their PRC2 status, whereas *DNMT3A* and *DNMT3B* expression is variable without any correlation to PRC2 status (Supplementary Fig. S2A and S2B). These data suggest that the selective DNMT1–PRC2 loss synthetic lethal interaction is through mechanisms distinct from selective *DNMT1* mutation or expression in MPNST tumor cells.

To validate whether PRC2 is a mediator of DNMT1 dependency in MPNST, we used two different *DNMT1*-specific shRNAs from the screen that efficiently depleted *DNMT1* mRNA expression across multiple MPNST cell lines (Supplementary Fig. S2C). We monitored the effect of shRNAs by a flow cytometry (FACS)–based growth competition assay between GFP-positive shRNA–expressing versus GFP-negative shRNA–nonexpressing MPNST cells; we observed significantly more rapid depletion of GFP-positive *DNMT1* shRNA–expressing cells in PRC2-loss compared with PRC2-WT MPNST cell lines (Fig. 1D). To confirm that enhanced sensitivity to *DNMT1* depletion is dependent on PRC2 status, we generated PRC2-isogenic human MPNST cells via CRISPR/Cas9-mediated knockout of *SUZ12* [single-guide (sg)*Con* (PRC2-WT) vs. sg*SUZ12* (PRC2-loss); Supplementary Fig. S2D and S2E]. Knockout of *SUZ12* did not markedly affect the protein expression of DNMT1, DNMT3A, or DNMT3B (Supplementary Fig. S2D and S2E). Importantly, we observed enhanced sensitivity to *DNMT1*-specific, but not *DNMT3A/B*-specific, knockdown in PRC2-loss compared with PRC2-WT MPNST isogenic background (Fig. 1E; Supplementary Fig. S2F–S2J). To evaluate the cross-dependency *in vivo*, we orthotopically transplanted luciferase-tagged PRC2-loss human MPNST cells stably expressing doxycycline-inducible shRNAs specific for *DNMT1*. We observed that *DNMT1*-specific shRNAs markedly suppressed MPNST tumor growth (Fig. 1F). These data confirmed the selective vulnerability of PRC2 inactivation to *DNMT1* depletion in cancer cells and tumors.

DNMT1-Targeted Therapy Exhibits Selective Antitumor Activity against PRC2-Loss Cancer

The RNAi screening results compelled us to evaluate whether the selective dependence on DNMT1 in PRC2-loss MPNST could be leveraged therapeutically. DNMT1 can be inhibited by the clinically available pan-DNMTi DAC, which is a nucleoside analogue that inhibits DNMT1, DNMT3A, and DNMT3B upon incorporation into DNA during S-phase (18). Alternatively, DNMT1 can be selectively and directly inhibited by a novel preclinical noncovalent, small-molecule, enzymatic inhibitor GSK3484862 (referred to as GSK862 hereafter; ref. 19). By dose–response analysis, we observed that PRC2 inactivation by CRISPR/Cas9-mediated knockout of *SUZ12* enhanced sensitivity to both DNMTis (Fig. 2A and B; Supplementary Fig. S3A). Long-term growth assays confirmed that DAC and GSK862 similarly exhibited enhanced cytotoxicity selective for PRC2-loss MPNST cells (Supplementary Fig. S3B and S3C). To further evaluate the role of cellular PRC2 activity on sensitivity to DNMTi therapy, we treated PRC2-isogenic MPNST cells with an EZH2 catalytic inhibitor (EPZ-6438; ref. 20) or an H3K27me3 binding pocket inhibitor of EED (EED226; refs. 20, 21). EZH2 and EED inhibitors effectively reduced H3K27me2/3 in PRC2-isogenic M3 cells and PRC2-WT M10 cells (Fig. 2C; Supplementary Fig. S3D) and led to enhanced cytotoxicity upon treatment by a DNMT1 inhibitor (DNMT1i; GSK862) in PRC2-WT MPNST cells (M3-sgCon and M10) but not in PRC2-loss cells (M3-sg*SUZ12*; Fig. 2D; Supplementary Fig. S3E). We further tested DNMTi therapy in established PRC2-isogenic ($Eed^{-/-}$ vs. $Eed^{f/-}$) murine MPNST cells derived from genetically engineered mouse models of MPNST that also harbor complete loss of *Nf1* and *Cdkn2a* (Fig. 2E). Similarly, we observed enhanced sensitivity to DNMTi in PRC2-loss ($Eed^{-/-}$) compared with PRC2-intact ($Eed^{f/-}$) murine MPNST cells (Fig. 2E). To further validate the selectivity of the DNMTi in PRC2-loss cells, we restored PRC2 activity by ectopically

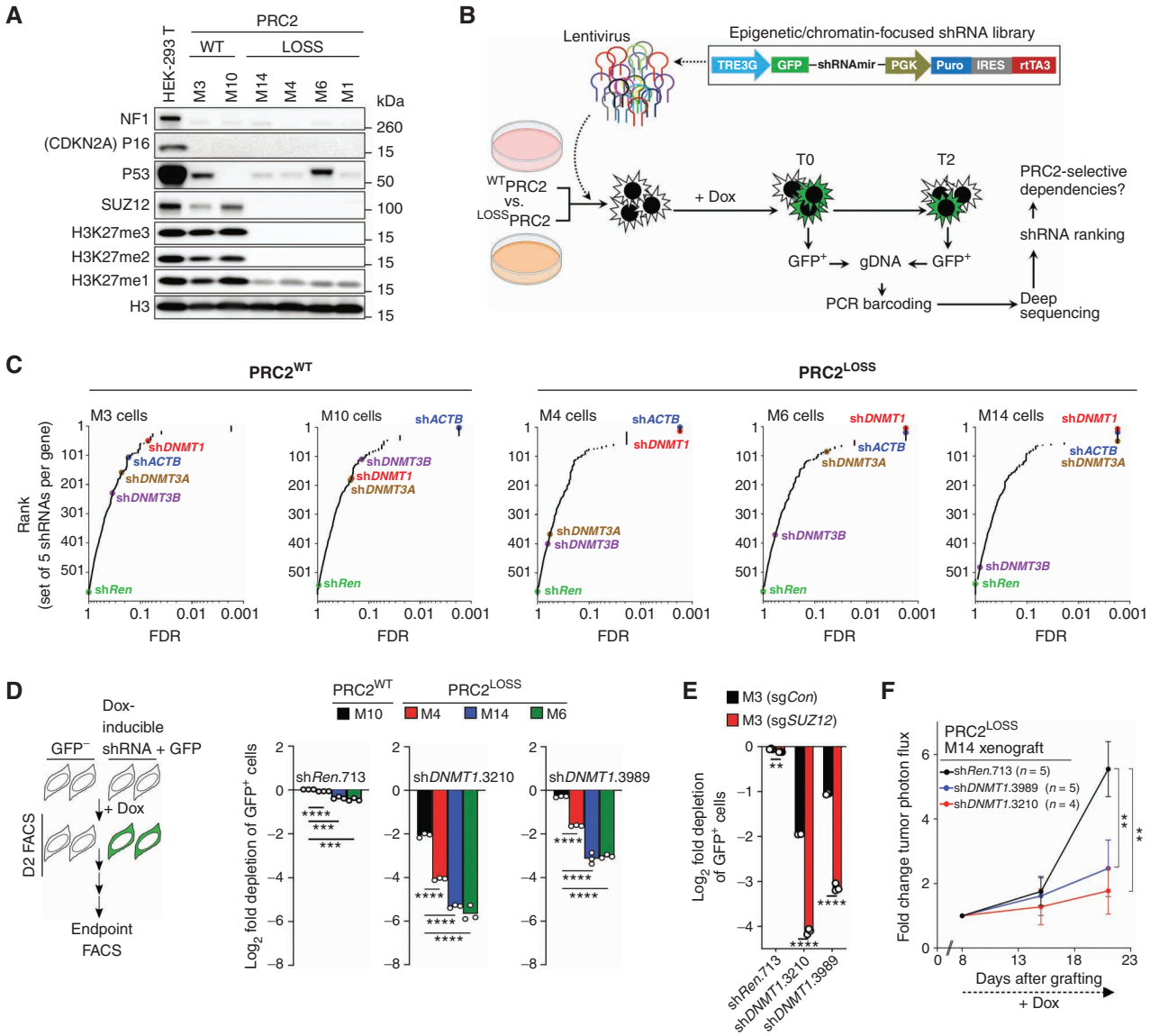

Figure 1. RNAi screen identifies increased *DNMT1* dependency conferred by PRC2 inactivation in MPNST. **A,** Western blot validation of human MPNST cell lines. **B,** Schematic of RNAi-based pooled dropout screen in PRC2-WT (M3 and M10) and PRC2-loss (M4, M6, and M14) MPNST cell lines. Dox, doxycycline. **C,** shRNA gene set rank and statistical significance (FDR) plot based on HiTSelect algorithm for shRNA depletion in each MPNST cell line. **D,** Growth competition assay by FACS using shRNA-linked GFP under DNMT1-specific perturbations (sh*DNMT1*.3210 and sh*DNMT1*.3989) compared with nontargeting control (sh*Ren*.713) in MPNST cell lines ($n = 3$ biological replicates). **E,** Validation of increased sensitivity to *DNMT1* knockdown in PRC2-loss setting via shRNA-linked GFP FACS-based growth competition assay in PRC2-isogenic MPNST cells [PRC2-WT = M3(sg*Con*) vs. PRC2-loss = M3(sg*SUZ12*)]. ($n = 3$ biological replicates) **F,** Luciferase bioluminescence-based growth curve over time for orthotopic human MPNST xenografts with doxycycline-inducible knockdown of *DNMT1*. Number (n) of animals per study group indicated in the figure. All error bars: mean ± SEM; Student two-tailed t test (**, $P < 0.01$; ***, $P < 0.001$; ****, $P < 0.0001$).

expressing *SUZ12* cDNA into *SUZ12*-null patient-derived MPNST cell lines and confirmed PRC2 activity (H3K27me3 and repression of PRC2 target genes; Supplementary Fig. S3F and S3G). We observed decreased sensitivity to DNMTi upon PRC2 restoration (Fig. 2F; Supplementary Fig. S3H), thus corroborating the PRC2 and DNMT pathway cross-dependence in MPNST. To evaluate the effect of DNMTi therapy *in vivo*, we treated various patient-derived MPNST xenograft tumor models with the pan-DNMTi (DAC). We observed that DAC exhibits selective antitumor activity against PRC2-loss tumors (Fig. 2G–I). To specifically inhibit DNMT1 *in vivo*, we utilized GSK3685032, a DNMT1-selective inhibitor that is structurally related to GSK862 but capable of *in vivo* inhibition of DNMT1 in mice (19). Consistent with GSK862 (Fig. 2F), GSK3685032 effectively inhibits *in vitro* growth of PRC2-loss MPNST cells but not when *SUZ12* is reexpressed (Supplementary Fig. S3I). Importantly, we observed that GSK3685032 potently inhibited orthotopic tumor growth of a PRC2-loss human MPNST cell line–derived xenograft (CDX; Fig. 2J). Collectively, these observations indicate that PRC2 inactivation selectively sensitizes MPNST cells and tumors to DNMT pathway inhibition.

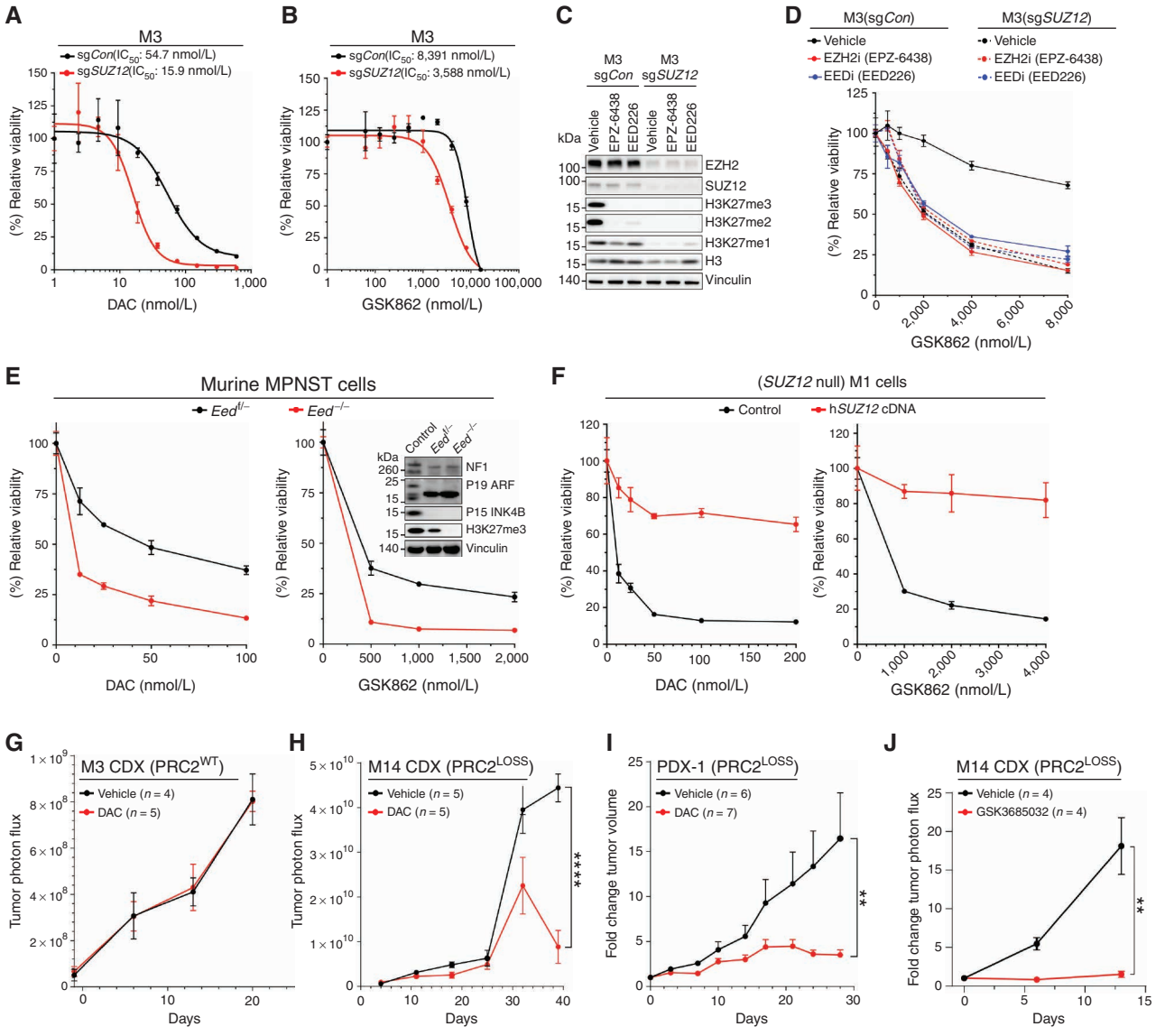

Figure 2. DNMT1-targeted therapy has a selective antitumor activity for PRC2-loss cancer. **A** and **B,** Dose–response curves and IC_{50} of a pan-DNMT inhibitor (DAC) or a DNMT1-selective inhibitor (GSK862) in *SUZ12*-isogenic MPNST cells: PRC2-WT = M3-sg*Con*; PRC2-loss = M3-sg*SUZ12* ($n = 3$ biological replicates per data point). **C,** Western blot analysis of *SUZ12*-isogenic cells treated with 3 μmol/L EPZ-6438 (an EZH2 inhibitor) or 5 μmol/L EED226 (an EED inhibitor). **D,** Dose–response curves of GSK862 in *SUZ12*-isogenic cells treated with an EZH2 inhibitor (EZH2i), an EED inhibitor (EEDi), or vehicle controls ($n = 3$ biological replicates per data point). **E,** Western blot validation and DNMTi (DAC and GSK862) dose–response curves for *Eed*-isogenic murine MPNST cells derived from *Nf1*$^{-/-}$;*Cdkn2a*$^{-/-}$;*Cdkn2b*$^{-/-}$ genetically engineered murine models ($n = 3$ biological replicates per data point). **F,** Dose–response curves of DAC and GSK862 in *SUZ12*-null human MPNST cells with or without PRC2 (*SUZ12*) restoration ($n = 3$ biological replicates per data point). **G** and **H,** Growth curves over time of orthotopically transplanted human PRC2-WT (M3) and PRC2-loss (M14) cell line–derived xenografts (CDX) in CB-17 SCID mice treated with DAC or vehicle control by luciferase bioluminescence imaging. Number (n) of animals per study group is indicated in the figure. **I,** Fold change tumor volume of subcutaneous PRC2-loss human MPNST patient-derived xenograft (PDX-1) treated with 5 mg/kg DAC or vehicle control. Number (n) of animals per study group is indicated in the figure. **J,** Luciferase bioluminescence-based growth curve over time of orthotopically transplanted human PRC2-loss M14 CDX in SCID mice treated with 45 mg/kg GSK3685032 or vehicle. The number (n) of animals per study group is indicated in the figure. All error bars: mean ± SEM; Student two-tailed t test (**, $P < 0.01$; ****, $P < 0.0001$).

PRC2 inactivation also occurs in other cancer types in addition to MPNST. To evaluate whether the selective antitumor activity of DNMT1i is applicable to other PRC2-loss cancers, we selectively analyzed several other cancer types, including melanoma, non–small cell lung cancer, and breast cancer. We pretreated the cancer cells with an EZH2 inhibitor and confirmed PRC2 inactivation by the loss of H3K27me2/3 marks (Supplementary Fig. S4A and S4B) and then assayed for sensitivity to the DNMT1i. We found that PRC2 inactivation via EZH2 inhibitor treatment augmented DNMT1i cytotoxicity in PRC2-WT human melanoma cell lines but not in non–small cell lung cancer or breast cancer cells (Supplementary Fig. S4C–S4E), indicating a cancer context–specific therapeutic vulnerability to DNMTi in PRC2 loss cancer.

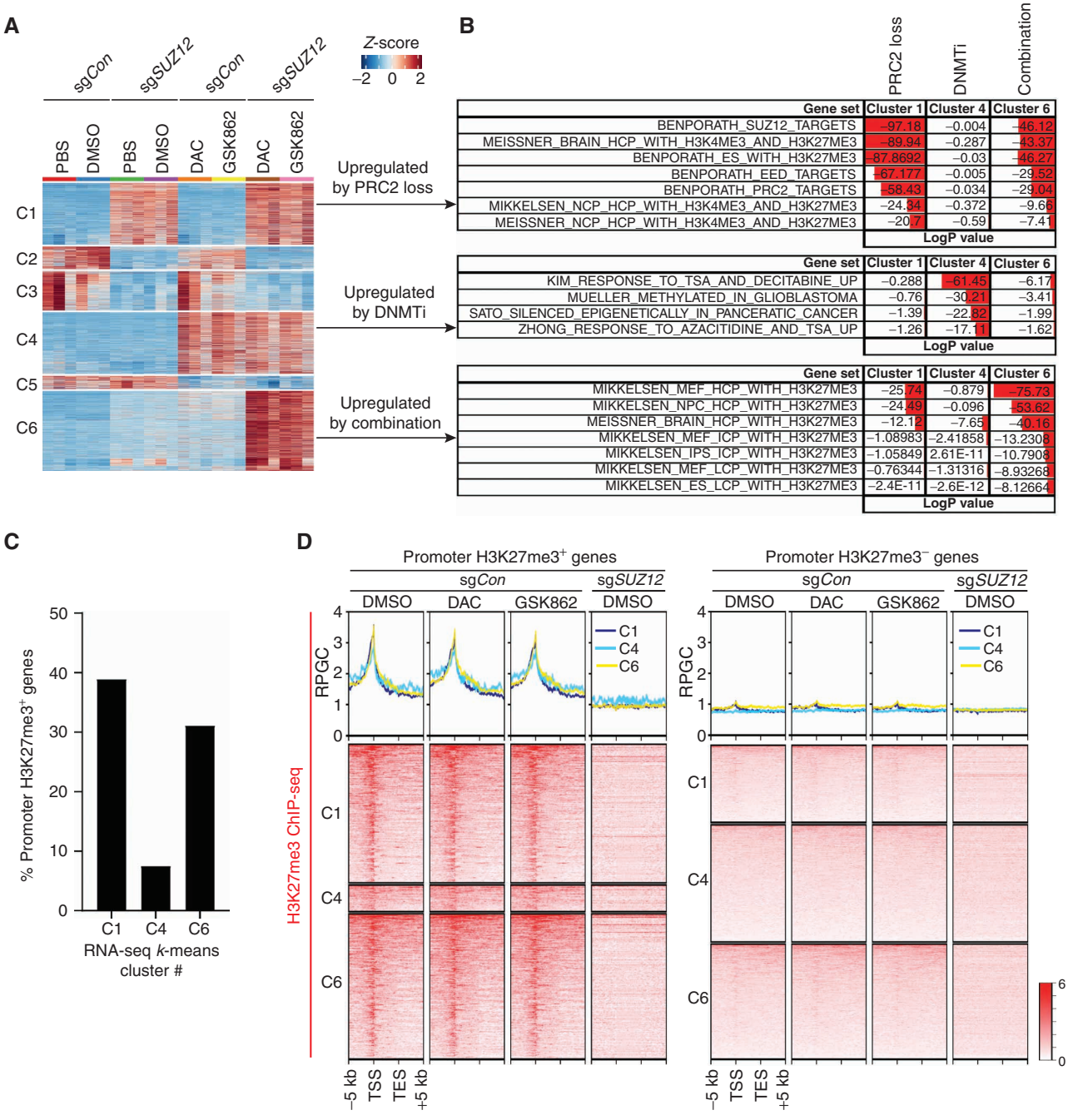

Figure 3. DNA methylation restricts the transcription of a subset of PRC2-regulated genes. **A,** *K*-means clustering of differentially expressed genes (FDR < 0.1 and $\log_2$ fold change >1.5) in *SUZ12*-isogenic M3 MPNST cells ± DNMTi. **B,** Gene set enrichment analysis identifies gene sets enriched by genes in RNA-seq *k*-means clusters 1 (C1), 4 (C4), and 6 (C6). **C,** Percentage of genes in C1, C4, and C6 that have a promoter enrichment of H3K27me3 by ChIP-seq in M3-sg*Con* cells. **D,** Enrichment profile of the average reads per genomic context (RPGC; top) and heat maps (bottom) of H3K27me3 ChIP-seq signals 5 kb upstream of the transcription start site (TSS) and 5 kb downstream of transcription end site (TES) of H3K27me3$^+$ and H3K27me3$^-$ genes in C1, C4, and C6 under various treatment conditions. One representative biological replicate is shown for each sample. (*continued on next page*)

CpG Island DNA Methylation Restricts Transcription of a Subset of PRC2/H3K27me3 Target Genes

Next, we investigated the molecular mechanisms underlying enhanced sensitivity to DNMT1-targeted therapy in PRC2-loss MPNST. We used RNA sequencing (RNA-seq), bisulfite sequencing (bisulfite-seq), and chromatin immunoprecipitation sequencing (ChIP-seq) to characterize and integrate transcriptome, methylome, and histone modification responses to DNMT1-targeted therapy in PRC2-isogenic MPNST cells. *K*-means clustering analysis of differentially expressed genes under different conditions in RNA-seq transcriptomes revealed six distinct clusters of genes (Fig. 3A). Reasoning that PRC2

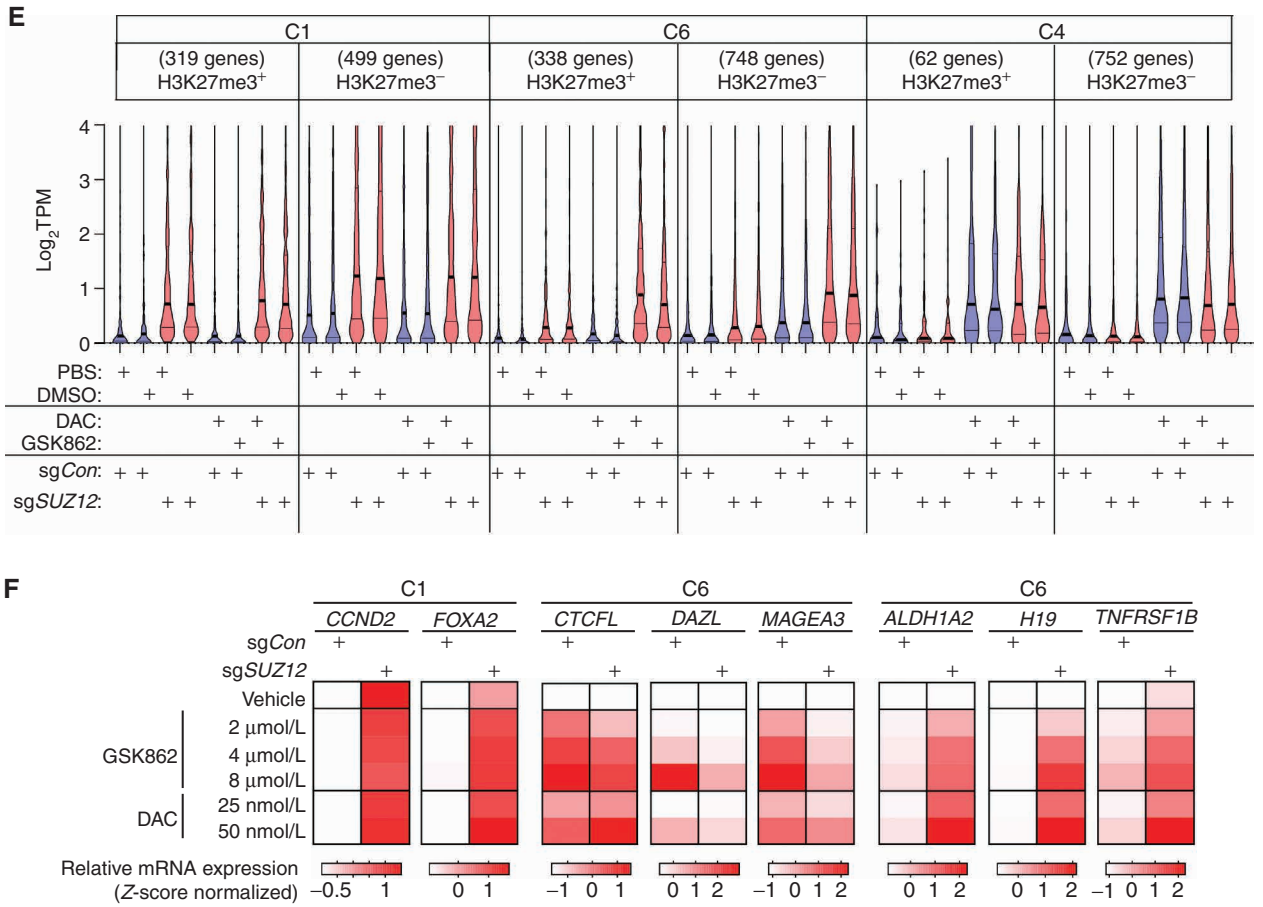

Figure 3. ***(Continued)*** **E,** RNA expression violin plot of genes in C1, C4, and C6 separated by promoter H3K27me3 enrichment status (±) under various treatment conditions. Transcripts per million (TPM) refers to normalized RNA expression. An average of two biological RNA-seq replicates is shown. Each violin has three lines inside. The middle thick line represents the median, and the upper and lower thin lines are the quartiles. **F,** Heat map of RNA expression by qRT-PCR of representative genes in C1, C4, and C6 in *SUZ12*-isogenic M3 cells under indicated treatment conditions. Note: *CCND2*, *FOXA2*, *ALDH1A2*, *H19*, and *TNFRSF1B* each have promoter H3K27me3 enrichment in M3(sg*Con*) cells. Average *Z*-score value of three technical replicates for each sample used to generate the heat map.

and DNMT1 are traditionally known for their roles in transcriptional silencing, we focused on genes upregulated in clusters C1, C4, and C6 (Fig. 3A). As expected, C1 genes exclusively upregulated by PRC2 loss were enriched for PRC2-related gene sets; C4 genes upregulated solely by DNMTi treatment led to the enrichment of previously published DNMTi-responsive gene sets (Fig. 3B). C6 genes were highly enriched for gene sets containing genes that have high-density CpG promoters and concurrent promoter H3K27me3 (Fig. 3B), which may suggest that C6 genes are coregulated by PRC2 and DNA methylation. In contrast, genes with intermediate- and low-density CpG promoters (ICP and LCP) and concurrent H3K27me3 were marginally enriched in C6 (Fig. 3B). ChIP-seq analysis of PRC2-WT MPNST cells confirmed that a large subset of C1 and C6 genes have promoter H3K27me3 enrichment at baseline that is unaffected by DNMTi treatment (Fig. 3C and D; Supplementary Fig. S5A). At the transcriptome level, most of the C1, C4, and C6 genes had low baseline mRNA expression regardless of H3K27me3 promoter enrichment, which is consistent with PRC2 and DNA methylation–mediated transcriptional silencing (Fig. 3E). Loss of PRC2 led to more robust transcriptional activation of C1 versus C6 genes (Fig. 3E). Similarly, DNMTi treatment led to more robust transcriptional activation of C4 versus C6 genes (Fig. 3E). The combined inactivation of PRC2 and DNMT pathways led to more robust transcriptional activation of C6 genes than by either perturbation alone (Fig. 3E).

We confirmed transcript expression dynamics elicited by PRC2 and DNMT pathway inhibition under various conditions and across multiple MPNST model systems for representative genes in C1, C4, and C6. First, we confirmed that these trends occurred in a dose-dependent manner in multiple PRC2-isogenic (sg*Con* vs. sg*SUZ12*) human MPNST cells *in vitro* (Fig. 3F; Supplementary Fig. S5B). Conversely, restoration of PRC2 activity dampened transcriptional activation of C6 genes by DNMTi therapy (Supplementary Fig. S5B). We confirmed that upregulation of C1 and C6 gene expression is dependent on loss of PRC2 enzymatic activity (Supplementary Fig. S5C). Moreover, these transcriptional changes were confirmed in PRC2-loss MPNST xenograft tumors *in vivo* with the shRNA-mediated knockdown of *DNMT1* (Supplementary Fig. S5D). These data suggest that DNA methylation restricts a subset of PRC2 targets in C6.

We next investigated DNA methylation dynamics via capture-based enrichment of approximately 3 million representative CpGs coupled with bisulfite-seq (Methyl-seq) after PRC2 and DNMT pathway perturbation. We obtained DNA methylation data for 2,357,491 CpGs and summarized the CpG methylation data binned into 370,075 tiling windows (regions) across the genome (Supplementary Fig. S6A). Principal component analysis (PCA) demonstrated that both DNMTi therapies (GSK862 and DAC) caused significant DNA methylation changes regardless of PRC2 status, and DNMTi-treated samples were readily separated from vehicle-treated samples by principal component 1 (PC#1; Supplementary Fig. S6B). The DNMTi-mediated DNA methylation changes were genome-wide across all regions, including promoters, exons, introns, and CPG islands (CGI) and shores (Supplementary Fig. S6C). In contrast, loss of PRC2 did not cause large-scale global reduction in DNA methylation at the regions we examined (Supplementary Fig. S6C). However, we identified a small number of differentially methylated regions (DMR; methylation difference ≥25%, $q < 0.01$) as a result of PRC2 loss—either hypomethylated ($n = 5{,}385$) or hypermethylated ($n = 3{,}496$) regions (Supplementary Fig. S6D). The percentages of hypermethylated and hypomethylated DMRs were similar at each genomic and CpG region (Supplementary Fig. S6E and S6F) and were associated with very few genes in RNA-seq *k*-means clusters C1, C4, and C6 (Supplementary Fig. S6G). These data suggest that PRC2-loss–mediated change in DNA methylation is not the main mechanism underlying the transcriptional silencing of C6 genes.

It is well established that DNA methylation at gene promoters is linked to repression of transcription initiation through various mechanisms (e.g., blockade of transcription factor binding, recruitment of corepressor complexes; ref. 22). We examined DNA methylation profiles spanning the transcription start site (TSS) to transcription end site (TES) of genes within each RNA-seq *k*-means cluster. As expected, the gene body and TES for all genes were DNA methylated, whereas most of the active genes in clusters 2, 3, and 5 (C2, C3, and C5) were DNA hypomethylated at their TSS/promoter regions (Supplementary Fig. S6H). Interestingly, genes preferentially upregulated by PRC2 loss (C1) had low levels of DNA methylation at their TSS/promoter regions; in contrast, genes preferentially upregulated by DNMTi (C4) or combined PRC2 loss and DNMTi (C6) had high or moderate levels of DNA methylation at their TSS/promoter regions, respectively (Supplementary Fig. S6H). We found a similar trend in DNA methylation profiles after separating genes in C1, C4, and C6 by the H3K27me3 promoter enrichment status (Fig. 4A). Within the vicinity of the TSS, we consistently found that most C6 genes had elevated DNA methylation at their promoter, CGIs, and shores compared with C1 genes (Fig. 4B).

Nearly ~70% of known gene promoters contain CGIs that are CpG-rich sites of transcription initiation when unmethylated but transcriptionally repressed when densely methylated (22). Moreover, H3K27me3 tends to be enriched at CGI sites (during *de novo* H3K27me3 methylation; ref. 23). We found that ~85% of H3K27me3$^+$ genes in C1 and ~80% of H3K27me3$^+$ genes in C6 have a promoter CGI (Fig. 4C). We quantitatively and visually confirmed that most of the C6 promoter CGI-containing genes had higher levels of DNA methylation compared with C1 genes (Fig. 4D and E). Inspection of genome tracks for representative H3K27me3$^+$ genes in C1 and C6 revealed that their promoter-associated CGIs both have H3K27me3/H3K4me3 enrichment, whereas DNA methylation is enriched for C6 but not for C1 genes (Fig. 4F). This is consistent with dual modes of transcriptional repression observed for C6 genes at their promoters by PRC2 and DNA methylation. These data suggest that in the absence of PRC2, robust transcription of a subset of all H3K27me3 decommissioned target genes is restricted by the presence of CGI DNA methylation at their promoters.

PRC2 Inactivation Amplifies DNMTi Therapy–Induced Viral Mimicry

We next investigated the biological signature output for C6 genes and its relevance to enhanced cytotoxicity to DNMTi therapy in PRC2-loss cancer context. We conducted gene ontology (GO) enrichment analysis for the six gene clusters in RNA-seq analysis and then performed hierarchical clustering of the GO terms to identify gene set signatures enriched by PRC2-loss and DNMTi coregulated genes in C6 (Fig. 5A). Immune gene sets related to innate immune response, interferon response, cytokines, and JAK/STAT signaling, as well as cell death signature gene sets were the most prominent (Fig. 5A and B). Consistent with these C6-enriched gene signatures, we found that DNMTi therapy induced immune response signaling pathways (e.g., phosphorylation of TBK1 and STAT1) and expression of proinflammatory cytokines in MPNST cells, which was further enhanced by PRC2 loss (Fig. 5C and D). These were of interest because previous studies in other cancer types delineated that pan-DNMTi therapy triggers viral mimicry through derepression of ERVs that form dsRNAs, which in turn primarily activate dsRNA sensor MDA5 to promote proinflammatory and antiviral innate immune response gene signatures (24, 25). Aberrant expression of retrotransposons, including ERVs (LTR retrotransposons), SINEs (short interspersed nuclear elements), and LINEs (long interspersed nuclear elements), can all activate cytosolic dsRNA sensors and proinflammatory and innate immune responses in the absence of viral pathogen infection (26–31). We therefore sought to determine if retrotransposon expression is regulated by PRC2 and DNA methylation. We first identified all retrotransposons (e.g., LTRs, LINEs, and SINEs) expressed at baseline and upon PRC2 loss and DNMTi treatment in our existing RNA-seq data (Supplementary Fig. S7A), followed by a differential analysis of expression (Fig. 5E and F). Although there were subsets of each retrotransposon class upregulated by a single perturbation of PRC2 loss or DNMTi, a substantial subset of each retrotransposon class was cooperatively upregulated by the combination of PRC2 loss and DNMTi treatment (Fig. 5E and F). The majority of retrotransposons measured in our system are expressed via passive cotranscription with genes or by pervasive intergenic transcription (32). Consistent with this, a subset of the differentially expressed retrotransposons were located within genes that are similarly upregulated by either PRC2 (C1) or DNMT1 (C4) perturbation or both (C6; Fig. 5G). Distribution analysis indicated that the median number of each retrotransposon class embedded within genes from RNA-seq clusters C1 to C6 were very similar (Supplementary Fig. S7B).

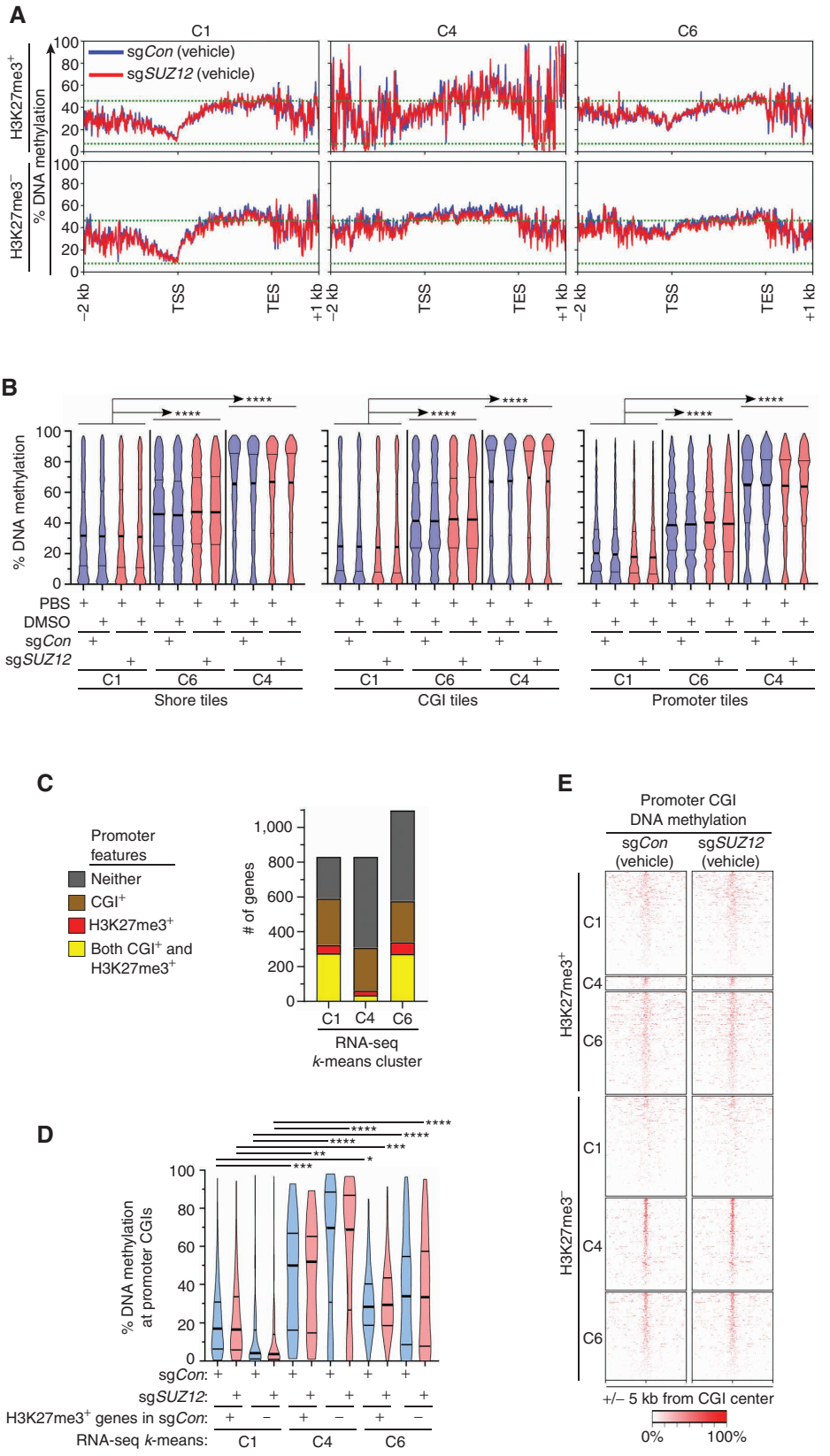

Figure 4. Promoter CGI DNA methylation associated with silencing of a subset of H3K27me3$^+$ and H3K27me3$^-$ genes in the absence of PRC2. **A,** DNA methylation profile plots for H3K27me3$^+$ and H3K27me3$^-$ genes in C1, C4, and C6 for M3(sg*Con*) and M3(sg*SUZ12*) cell lines. Combined average of two DMSO-treated biological replicates and two PBS-treated biological replicates is shown for each cell line. **B,** Tile (region) DNA methylation violin plot for CpG shores, CGIs, and promoters of genes in C1, C4, and C6. Average of two biological replicates per sample is shown. Each violin has three lines inside. The middle thick line represents the median, and the upper and lower thin lines are the quartiles. One-way ANOVA test with Benjamini–Hochberg FDR correction (****, $q < 10^{-14}$). **C,** Number of genes in specified RNA-seq *k*-means clusters that have a CGI and/or H3K27me3 enrichment at their respective promoters. **D,** Violin plot of DNA methylation at promoter CGIs in *SUZ12*-isogenic M3 cells. Average of two biological replicates per sample is shown. Each violin has three lines inside. The middle thick line represents the median, and the upper and lower thin lines are the quartiles. One-way ANOVA test with Benjamini–Hochberg FDR correction (*, $q < 10^{-4}$; **, $q < 10^{-5}$; ***, $q < 10^{-6}$; ****, $q < 10^{-14}$). **E,** DNA methylation density heat map for promoter CGI-containing genes. Combined average of two DMSO-treated biological replicates and two PBS-treated biological replicates is shown for each cell line. (*continued on following page*)

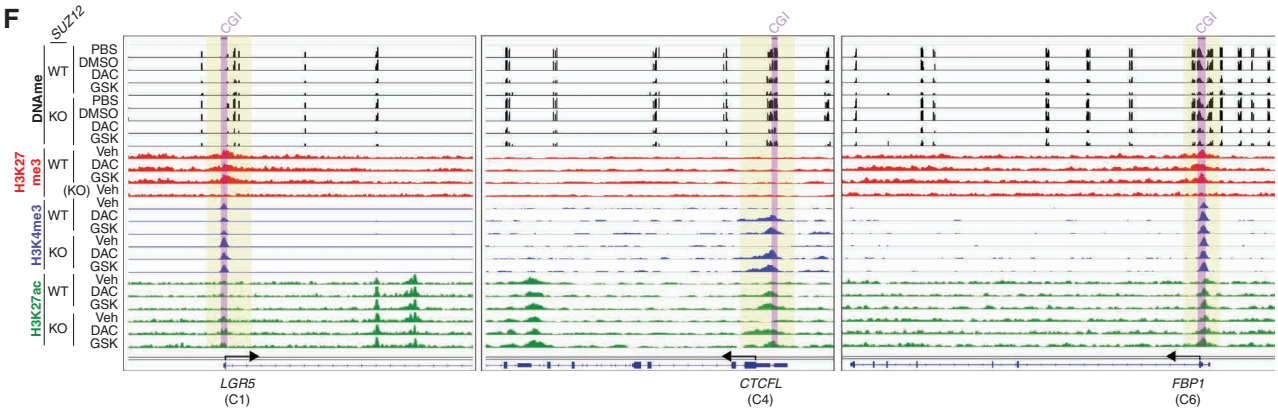

Figure 4. ***(Continued)*** **F,** ChIP-seq (H3K27me3, H3K4me3, and H3K27ac) and DNA methylation profiles of representative genes in C1, C4, and C6 in *SUZ12*-isogenic M3 cells (WT = sg*Con*; knockout = sg*SUZ12*). Promoter CGI regions are shaded in purple. One representative biological replicate is shown for each sample.

These differentially expressed retrotransposons did not have differential enrichment of histone modifications (H3K27me3, H3K27ac, H3K4me3) and DNA methylation, as they were distributed at various genomic locations without apparent biases (Supplementary Fig. S7C). We confirmed that the expression of each retrotransposon class and associated gene could be similarly upregulated by PRC2 and DNMT1 perturbations, which might suggest that these retrotransposons were passively cotranscribed with genes (Supplementary Fig. S7C and S7D). These data suggest that PRC2 inactivation augments DNMTi-mediated expression of retrotransposons to elicit a stronger viral mimicry transcriptional cell state than by DNMTi therapy or by PRC2 loss alone, which may contribute to the enhanced cytotoxicity of the combinatorial perturbations.

PRC2-Loss Selective Cell Death via DNMTi Therapy Is Mediated by the dsRNA Sensor PKR

Historically, DNMTi (e.g., 5-azacytidine or DAC) therapy is largely cytostatic at clinically achievable concentrations and has limited activity in solid tumors (33, 34). Previous preclinical studies with pan-DNMTis in which retrotransposons were derepressed also exhibited modest antiproliferative activity (24, 25). In contrast, we noted increased enrichment of cell death gene signatures in response to DNMTi in the PRC2-loss cancer context (Fig. 5A and B). We consistently observed that PRC2 inactivation in various cancer models converted a mostly cytostatic response into robust cytotoxicity upon DNMTi therapy via caspase-dependent programmed cell death (Fig. 6A–D; Supplementary Fig. S8A and S8B). These observations led us to investigate whether enhanced expression of retrotransposons by the combination of PRC2 loss and DNMTi therapy mediates the profound cytotoxicity upon DNMTi therapy. It is reported that retrotransposons can be reverse transcribed into double-stranded DNA (dsDNA) that can trigger innate immune responses via the cGAS/STING pathway (35). Hence, we examined both dsDNA- and dsRNA-sensing pathways in DNMT1i-mediated cytotoxicity in the PRC2-loss context.

Cytosolic dsDNA can be sensed by various cytosolic dsDNA sensors (e.g., AIM2 and cGAS; ref. 36). AIM2 is typically expressed in immune cells (The Human Protein Atlas) and involves the ASC adapter and Caspase 1 for downstream activation of inflammasomes (37); AIM2, ASC, and Caspase 1 were all expressed at very low levels in MPNST cells with or without perturbation of PRC2 or DNMT1, suggesting that this pathway may not be relevant to MPNST. Depletion of STING (a key effector downstream from cGAS) was insufficient to rescue DNMTi cytotoxicity in PRC2-loss MPNST cells (Supplementary Fig. S9A and S9B).

Retrotransposons, including ERVs, LINEs, and SINEs, can form dsRNAs that are recognizable by various cytosolic dsRNA sensor proteins including RIG-I–like receptors (e.g., RIG-I and MDA5), oligoadenylate synthases (OASes; e.g., OAS1/2/3), and PKR, which can lead to activation of innate immune responses and antiproliferative/survival outcomes (ref. 27; Fig. 6E). To determine which dsRNA sensor mediates the lethality of DNMTi in the PRC2-loss cancer context, we engineered knockout of *MAVS* (a key signaling adapter downstream of RIG-I and MDA5; ref. 27), *RNaseL* (a key effector activated redundantly by OAS1/2/3; ref. 27), or PKR (27) in PRC2-isogenic cells (Fig. 6E and F). Only knockout of *PKR* was able to partially rescue DNMTi-induced cytotoxicity in the PRC2-loss context (Fig. 6G). Moreover, additional knockout of *RNaseL* and/or partial knockout of *MAVS* in sg*PKR* cells did not further rescue cells from DNMTi therapy, which suggests PKR as the key cytosolic dsRNA sensor mediating DNMTi cytotoxicity (Supplementary Fig. S10A and S10B). Binding of dsRNA to PKR has been reported to cause subsequent downstream phosphorylation of eIF2α, which inhibits cap-dependent mRNA translation, and increase ATF4 protein level through non–cap-dependent protein translation (38, 39). Consistently, PKR signaling manifested by downstream signaling effect was further enhanced by DNMTi treatment in the PRC2-loss context (e.g., phosphorylation of TBK1, STAT1, and eIF2α increased ATF4 protein levels); this is partially rescued by PKR knockout, thus corroborating the augmented PKR pathway activation and effects with DNMTi treatment in the PRC2-loss context (Fig. 6H). Collectively, these findings suggest that loss of PRC2 creates a specific therapeutic vulnerability to DNMTi through the augmented expression of retrotransposons and subsequent PKR activation (Fig. 6I).

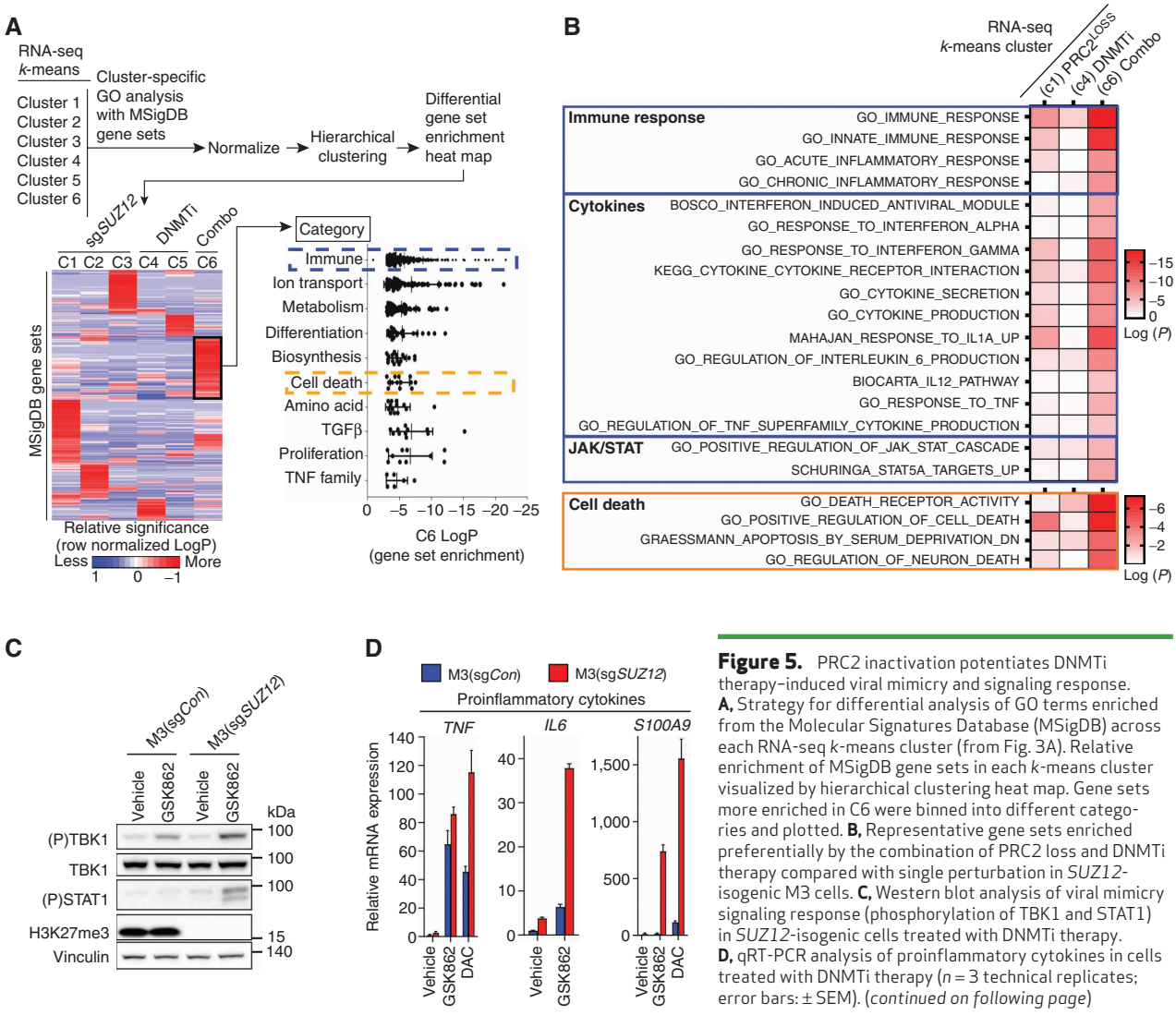

Figure 5. PRC2 inactivation potentiates DNMTi therapy–induced viral mimicry and signaling response. **A,** Strategy for differential analysis of GO terms enriched from the Molecular Signatures Database (MSigDB) across each RNA-seq *k*-means cluster (from Fig. 3A). Relative enrichment of MSigDB gene sets in each *k*-means cluster visualized by hierarchical clustering heat map. Gene sets more enriched in C6 were binned into different categories and plotted. **B,** Representative gene sets enriched preferentially by the combination of PRC2 loss and DNMTi therapy compared with single perturbation in *SUZ12*-isogenic M3 cells. **C,** Western blot analysis of viral mimicry signaling response (phosphorylation of TBK1 and STAT1) in *SUZ12*-isogenic cells treated with DNMTi therapy. **D,** qRT-PCR analysis of proinflammatory cytokines in cells treated with DNMTi therapy ($n = 3$ technical replicates; error bars: ± SEM). (*continued on following page*)

DISCUSSION

Despite the clinical success of targeting PRC2 in PRC2-dependent cancers (40, 41), therapeutically targeting tumor suppressor loss in PRC2-loss cancers remains challenging. In this study, we found that PRC2 inactivation augments the cytotoxicity of DNMTi therapy in MPNST. We found that PRC2 inactivation via EZH2 inhibitor treatment augmented DNMT1i cytotoxicity in PRC2-WT human melanoma cell lines but not in non–small cell lung cancer or breast cancer cells, suggesting a cancer lineage context–specific enhancement of DNMT1i therapy by PRC2 inhibition. This suggests that the combined strategy of targeting both PRC2 and DNMT1 may have a therapeutic window in selective cancer types, which will require future investigation.

DNMT1 is the sole methylation maintenance enzyme and is important in maintaining genomic integrity and regulating transcription of a subset of genes and retrotransposons together with other chromatin factors (17, 42, 43). DNMT3A and DNMT3B have overlapping functions, can both establish *de novo* methylation, and are variably expressed in different tissue types and cellular states (17, 44). In MPNST, *DNMT3A* or *3B* is not consistently expressed. For example, *DNMT3A* was only modestly expressed in many MPNST cell lines, whereas *DNMT3B* was barely expressed in MPNST cell lines. The low sensitivity to either *DNMT3A* or *3B* perturbation alone may be due to their functional redundancy but is more likely due to their functional differences from DNMT1.

Loss of any one of the PRC2 core components (*SUZ12*, *EED*, or *EZH2*) is sufficient to augment DNMTi cytotoxicity in MPNST, which suggests a critical role for PRC2 histone methyltransferase activity for the phenotype. In support of this, our integrative genomic analyses revealed dual regulation of a subset of H3K27me3 gene targets by the PRC2 and DNMT pathways. Specifically, upon PRC2 loss in MPNST, DNMT1-mediated DNA methylation is associated with restricted expression of a subset of H3K27me3 gene targets, whereas the transcription of non–DNMT-regulated H3K27me3 gene targets is robustly activated by PRC2 loss alone. These findings are consistent with human embryonic stem cells in which loss of TET enzymes leads to the acquisition of promoter DNA methylation at H3K27me3 target genes, which subsequently

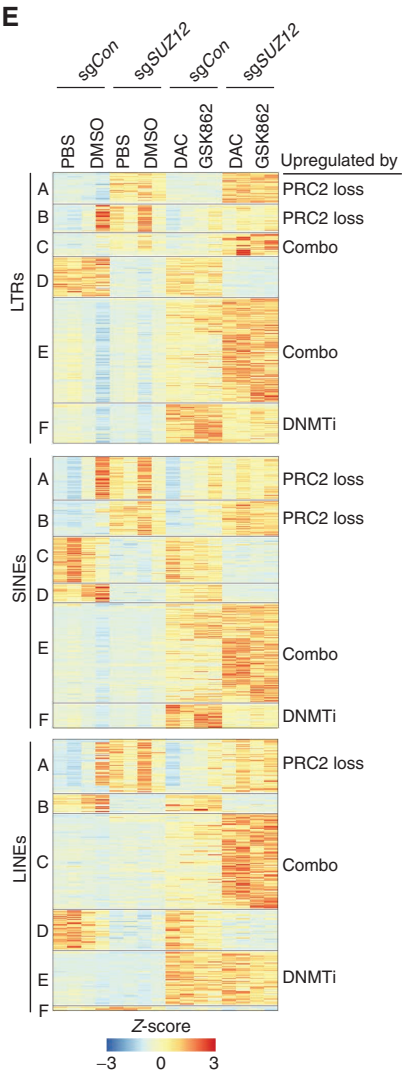

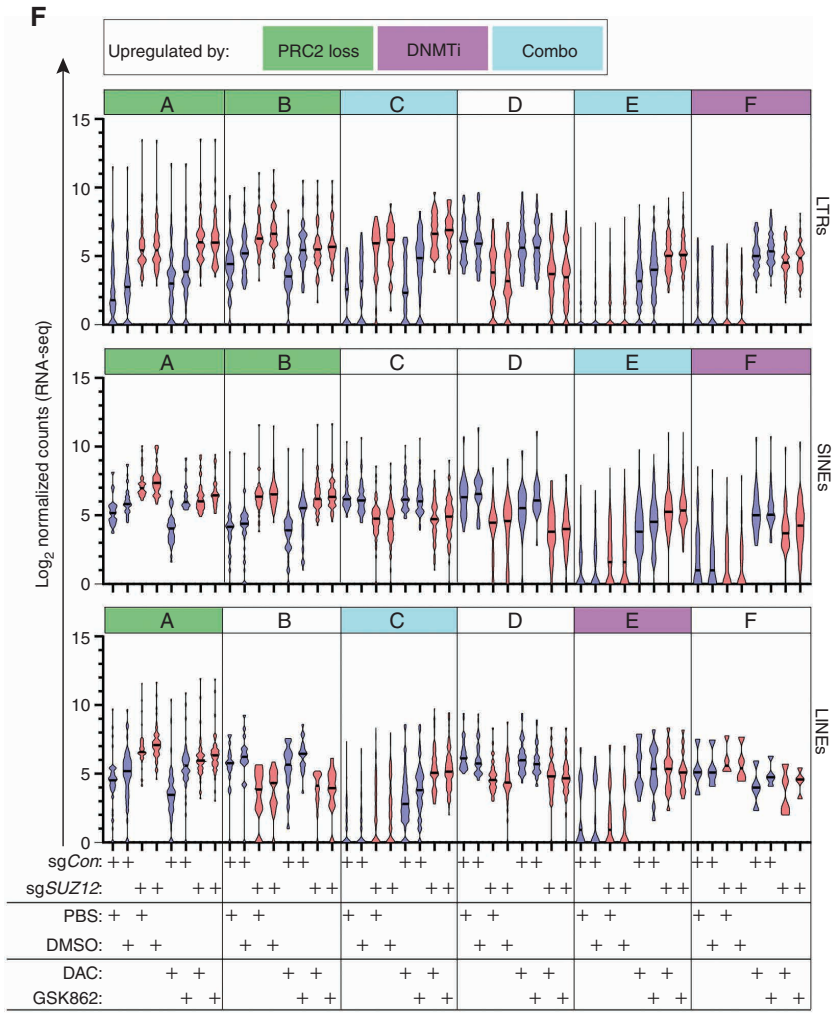

G

Upregulated by:

PRC2 loss | DNMTi | Combo

LTRs		% of LTRs located within genes in RNA-seq *k*-means cluster		
k-means cluster	# of LTRs	C1	C4	C6
A+B	98	**18.4**	1	12.2
F	67	0	**35.8**	0
C+E	215	2.3	20.9	**30.7**

SINEs		% of SINEs located within genes in RNA-seq *k*-means cluster		
k-means cluster	# of SINEs	C1	C4	C6
A+B	109	**20.2**	0.9	3.7
F	35	0	**17.1**	0
E	141	1.4	24.1	**33.3**

LINEs		% of LINEs located within genes in RNA-seq *k*-means cluster		
k-means cluster	# of LINEs	C1	C4	C6
A	54	**24.1**	0	1.9
E	54	0	**48.1**	0
C	96	6.3	16.7	**30.2**

Figure 5. ***(Continued)*** **E,** *K*-means clustering analysis for differentially expressed retrotransposons in *SUZ12*-isogenic M3 cells treated under various conditions. **F,** RNA expression violin plots for differentially expressed retrotransposons in *SUZ12*-isogenic M3 cells under various treatment conditions. Average of two biological RNA-seq replicates per sample is shown. Each violin has three lines inside. The middle thick line represents the median, and the upper and lower thin lines are the quartiles. **G,** Percentage of differentially expressed retrotransposons that are located within genes (−1 kb of gene starts to +1 kb of gene ends) from RNA-seq *k*-means clusters (C1, C4, and C6).

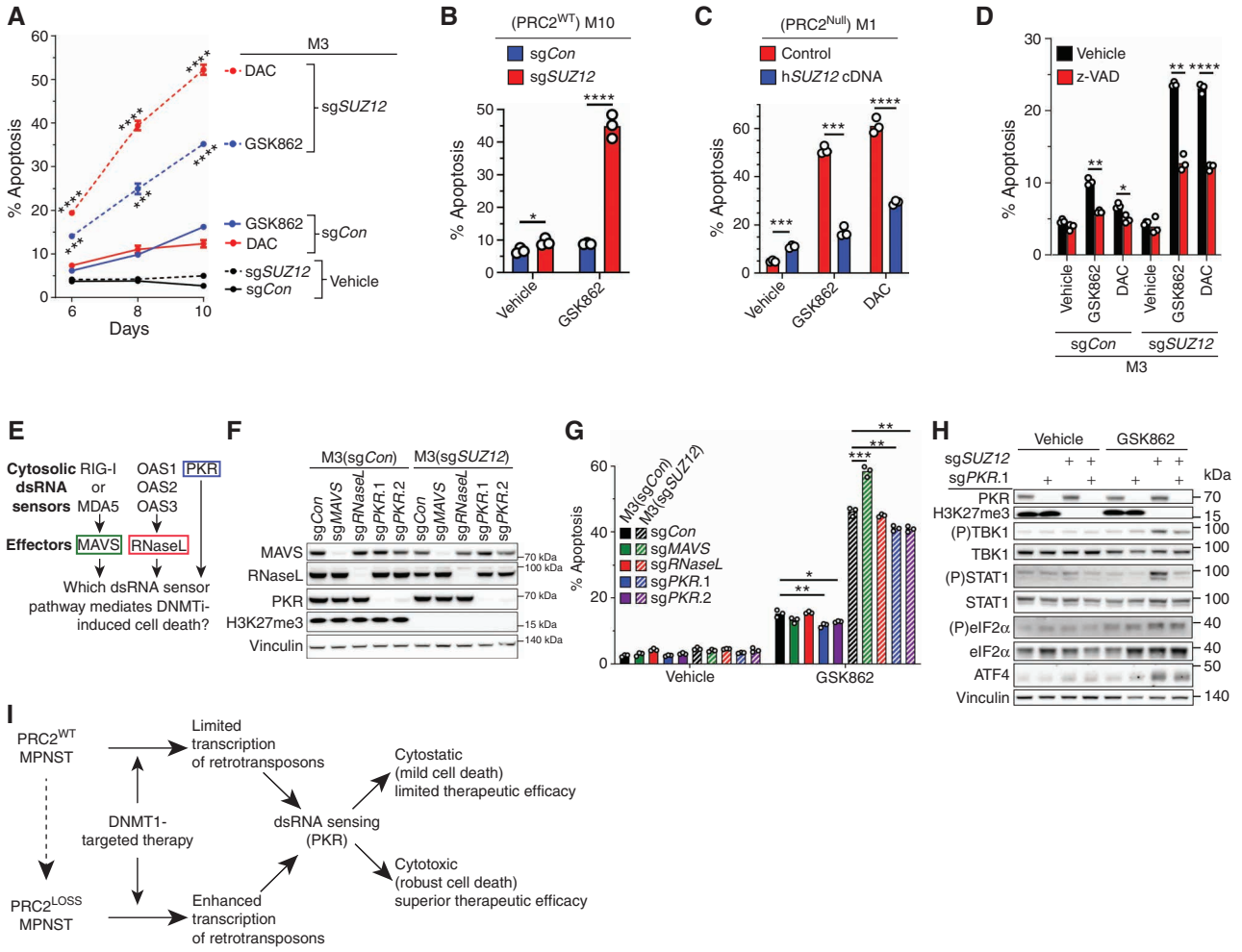

Figure 6. PRC2 inactivation enhances DNMTi-induced programmed cell death via PKR-mediated viral mimicry sensing. **A–C,** FACS analysis for Annexin V$^+$ apoptotic cells ($n = 3$ biological replicates). **D,** FACS analysis of DNMTi-induced apoptosis (Annexin V$^+$) in cells treated ± pan-caspase inhibitor (z-VAD-FMK; $n = 3$ biological replicates). **E,** A schematic of several main dsRNA sensors and their direct effectors. **F,** Western blot validation of CRISPR/Cas9-mediated knockout of *MAVS*, *RNaseL*, and *PKR*. **G,** FACS analysis for apoptosis (Annexin V$^+$) in 3 μmol/L GSK862-treated *SUZ12* isogenic M3 cells (± knockout of either *MAVS*, *RNaseL*, or *PKR*; $n = 3$ biological replicates). **H,** Western blot of GSK862-mediated induction of PKR signaling and attenuation by *PKR* knockout in *SUZ12*-isogenic M3 cells. **I,** Proposed model of mechanisms underlying enhanced therapeutic efficacy of DNMTi therapy in cancer with PRC2 inactivation. All data presented as the mean ± SEM; Student two-tailed *t* test (*, $P < 0.05$; **, $P < 0.01$; ***, $P < 0.001$; ****, $P < 0.0001$).

maintains their silencing after H3K27me3 removal upon cellular differentiation (45). PRC2 can function as an oncogenic driver or tumor suppressor depending on the cancer cell context. Given that PRC2 is a bona fide tumor suppressor in MPNST pathogenesis (9–11), our data suggest that DNA methylation restricts transcription of a subset of H3K27me3 gene targets that are anti-fitness in tumorigenesis and points to potential context-dependent therapeutic opportunities.

Pan-DNMTis (DAC and 5-azacytidine) have been shown to induce innate immune signaling and modest antiproliferative effects via activation of RIG-I/MDA5-dependent dsRNA sensing and subsequent viral mimicry in various solid tumor cell lines without particular molecular features (24, 25). Although pan-DNMTis have been shown to have antiproliferative effects in various cancer cell lines *in vitro* (34, 46–48), they have had limited clinical activity as single agents, likely due to the lack of cytotoxic effects in the nonselective context of most solid tumors (34, 48, 49). Our study through a nonbiased RNAi-based screen identified DNMT1 as a synthetic lethal interaction candidate with PRC2 loss. Using the pan-DNMTi (at low doses that minimize off-target effects) and a novel DNMT1-selective small-molecule inhibitor (19), we demonstrated that the DNMTi can induce robust caspase-dependent programmed cell death *in vitro* and potent antitumor effects *in vivo* in the PRC2-loss cancer context, which suggests a potential therapeutic opportunity. We further demonstrated that DNMTi cooperatively induces an augmented expression of various retrotransposon elements (RE), including ERVs/LTRs, LINEs, SINEs, which in turn activates the proinflammatory and innate immune signaling responses, probably through multiple dsRNA sensing mechanisms (RIG-I/MDA5, PKR, OASes, etc.). However, for the DNMTi-mediated programmed cell death effects in the PRC2-loss MPNSTs, we focused on robustly expressed dsRNA sensors in MPNST (e.g., RIG-I/MDA5, RIG, and OASes). Among them, PKR, but not RIG-I/MDA5/MAVS or OAS/RNaseL, mediated dsRNA sensing and activation of downstream signaling, which

were required for robust antitumor effects, in contrast to previous studies (24, 25, 50). It is worth noting that different dsRNA sensors have differential RNA substrate binding specificity based on dsRNA features, including length, secondary structures, local mismatches, and noncanonical pairs (27, 51). Analysis of how those features dictate which dsRNA sensing pathway mediates an antitumoral outcome in response to DNMTi may be the focus of future investigations.

Our study provides the scientific rationale for clinically evaluating DNMTi in patients with PRC2-loss MPNST who currently have an unmet clinical need. To date, most preclinical therapeutic candidates for MPNST have been derived by insights from PRC2-WT genetically engineered murine MPNST models and/or limited human MPNST preclinical *in vivo* models (52–62). Our study leveraged multiple authenticated *in vitro* and *in vivo* human patient-derived models of PRC2-WT and PRC2-loss MPNST as well as murine models to identify and validate DNMT1 pathway inhibition as a potential therapeutic strategy for PRC2-loss MPNST. Several pan-DNMTis—for example, DAC, 5-azacytidine, and oral combination of DAC and cedazuridine—have been approved by the FDA for the treatment of myelodysplastic syndromes (18, 63, 64). Based on our data, we have just started an investigator-initiated trial of ASTX727 (oral combination of DAC and cedazuridine) in patients with PRC2-loss MPNST (ClinicalTrials.gov: NCT04872543). Ideally, a clinical evaluation of DNMT1-specific inhibitors that minimize the off-target effects should be considered in cancers with the PRC2-loss context. An orally bioavailable DNMT1-selective inhibitor has recently been shown in murine models to effectively reduce DNA methylation and induce tumor regression while being well tolerated without adverse hematologic toxicity (19), which may circumvent the known side effects of myelosuppression of DAC (18). Historically, pan-DNMTis have had limited activity in solid tumors (65). Our study identified the PRC2-loss cancer context as a selective therapeutic vulnerability to DNMTi. PRC2 loss can be readily identified by IHC staining of H3K27me3 and FDA-approved molecular biomarker testing assays, such as Foundation One (Foundation Medicine, Inc.) or MSK-IMPACT (66), which may be useful for the biomarker-driven clinical investigation of pan-DNMT– and DNMT1-targeted therapeutics in solid tumors.

METHODS

Cell Lines

NF1 patient-derived human MPNST cell lines M14 (ST88-14, RRID:CVCL_8916) and M10 (MPNST1) were kind gifts provided by Jonathan A. Fletcher (Brigham and Women's Hospital, Harvard Medical School). NF1 patient-derived human MPNST cell lines M1, M3, M4, and M6 were kind gifts developed by William L. Gerald and Xiaoliang L. Xu at Memorial Sloan Kettering Cancer Center (MSKCC). COLO800 cells (RRID:CVCL_1135) were provided by the laboratory of Joan Massagué and were cultured in Roswell Park Memorial Institute medium (RPMI) media. 501mel cells were provided by the laboratory of Levi Garraway and were cultured in RPMI. SKMEL-28 (RRID:CVCL_0526) are patient-derived melanoma cell lines established at MSKCC and were cultured in RPMI. A549 (RRID:CVCL_0023), NCI-H358 (RRID:CVCL_1559), and NCI-H2228 (RRID:CVCL_1543) were provided by the laboratory of Charles M. Rudin and were cultured in RPMI. MCF-7 (RRID:CVCL_0031) and MDA-MB-468 (RRID:CVCL_0419) were provided by the laboratory of Sarat Chandarlapaty and were cultured in RPMI. *SUZ12* isogenic M10 and M3 MPNST cells were generated by CRISPR/Cas9 targeting of *SUZ12* followed by isolation and validation of single-cell clones. At least five single-cell clones of sg*Con* or sg*SUZ12* were respectively pooled to create cell lines for experiments. *Eed*-isogenic mouse MPNST cells were generated as follows: $Eed^{f/f}$ mice (67, 68) were bred with PLP-CreERT::$Nf1^{f/f}$;$Cdkn2a^{f/f}$ mice. $Nf1^{-/-}$;$Cdkn2a^{-/-}$;$Eed^{f/-}$ cells were cultured from lumbar nerves in tamoxifen-treated PLP-CreERT::$Nf1^{f/f}$;$Cdkn2a^{f/f}$;$Eed^{f/f}$ mice. *Eed*-null cells were generated by infection with adenovirus-Cre *in vitro*. *Eed*-isogenic cells were infected with sgRNA lentiviruses for additional knockout of *Cdkn2b* followed by subcutaneous implantation into CB-17 SCID mice (Taconic, RRID:IMSR_TAC:cb17sc), and upon malignant tumor formation, *Eed*-isogenic murine MPNST primary cell lines ($Nf1^{-/-}$;$Cdkn2a^{-/-}$;$Cdkn2b^{-/-}$) were derived from tumors. Histopathology was verified by C.R. Antonescu. All MPNST cell lines (human and mouse) and HEK-293T cells (ATCC; cat. #CRL-3216, RRID:CVCL_0063) were cultured in DMEM:F-12 (1:1) high-glucose media. All cell culture media contained 10% FBS, L-glutamine (2 mmol/L), penicillin (100 U/mL), and streptomycin (100 μg/mL) with the exception of human MPNST cell lines, which were cultured in advanced DMEM/F12 media (Gibco) supplemented with 15% FBS, 2 mmol/L L-glutamine, penicillin (100 U/mL), and streptomycin (100 μg/mL) for shRNA library screening. All cells were cultured at 37°C in 5% CO_2 and tested negative for *Mycoplasma* (Applied Biological Materials Inc.; cat. #G238) every 3 months.

Virus Packaging and Infection

Lentiviral transfer plasmid plus packaging plasmids psPAX2 (gift from Didier Trono, Addgene Plasmid #12260, RRID:Addgene_12260) and pCMV-VSV-G (gift from Bob Weinberg, Addgene Plasmid #8454, RRID:Addgene_8454) were cotransfected intro HEK-293T cells (ATCC; cat. #CRL-3216, RRID:CVCL_0063) via X-tremeGene 9 reagent (Millipore Sigma; #6365787001). Two days later, viral media were filtered through a 0.45-μm sterile syringe filter and stored at −80°C. For infection, the thawed virus was mixed with culture media +8 μg/mL polybrene (Millipore Sigma; #107689) to infect cells overnight, followed by removal of virus media. Virus-infected cells were selected with appropriate antibiotics 2 days after infection.

shRNA Library Screening

A doxycycline-inducible pooled human epigenome-focused lentiviral shRNA plasmid library in the LT3GEPIR mir-E backbone (Fig. 1B; Supplementary Table S2; ref. 69) targeting 565 genes (5 shRNAs per gene) was obtained from the Gene Editing and Screening Core Facility (MSKCC). HEK-293T cells were cotransfected with packaging plasmids to produce lentivirus for the shRNA library. Target cell lines were infected with library lentiviruses at ~10% transduction efficiency, followed by selection with 2 μg/mL puromycin for 4 days, and maintenance/expansion of cells at 3,000× shRNA representation under 1 μg/mL puromycin for an additional 7 days. For screening, cells were maintained at a minimum of 1,000× shRNA representation. shRNAs were induced with 1 μg/mL doxycycline, and GFP+ shRNA-expressing cells were isolated by FACS at passage doubling 1 and 15 followed by genomic DNA isolation with the Gentra Puregene cell kit (Qiagen). Sequencing libraries were prepared by subjecting 18 μg (1.2 μg × 15 reactions) of genomic DNA (~1,000× shRNA representation) to PCR-based barcoding and amplification with the AmpliTaq Gold PCR kit (Thermo Fisher Scientific). See Supplementary Table S3 for a list of barcode adapter primers. Parallel PCR reactions were pooled and purified by a column-based PCR purification kit (Qiagen), followed

by 30-minute incubation at 37°C with exonuclease I (New England BioLabs) to digest excess single-stranded DNA primers, subsequent separation by agarose gel electrophoresis, and gel extraction via a gel purification kit (Qiagen). Purified libraries (PCR product) were subjected to single-end, 50-bp high-throughput sequencing on an Illumina HiSeq2500 platform. All resulting FASTQ files passed quality control by FastQC (RRID:SCR_014583; https://www.bioinformatics.babraham.ac.uk/projects/fastqc/). Sequencing reads were trimmed with Cutadapt (RRID:SCR_011841; ref. 70) to keep only 22-mer shRNA guide sequences that were subsequently mapped to the shRNA library guide sequence reference file using bowtie2 (RRID:SCR_016368; ref. 71). shRNA read counts were quantified by edgeR (RRID:SCR_012802; ref. 72). Ranking of each set of five shRNAs per gene in the library was done for depletion with HiTSelect (20). See Supplementary Table S1 for resulting shRNA ranking data.

See Supplementary Table S4 for drugs, chemicals, and regents used in this study. Cells were treated with low-dose DAC for 4 consecutive days in all *in vitro* experiments.

Dose–Response and Cellular Growth/Viability Assays

ATP CellTiter-Glo 2.0 cell viability assays (Promega) were performed as previously described (58, 73) to generate dose–response and growth curves in Fig. 2 and Supplementary Fig. S2. All data are plotted with GraphPad (Prism, RRID:SCR_002798).

Animal Studies

Animal experiments were carried out in accordance with protocols approved by the MSKCC Institutional Animal Care and Use Committee and were in compliance with relevant ethical regulations regarding animal research. For DAC studies on human MPNST xenograft-bearing CB-17 SCID mice (Taconic, RRID:IMSR_TAC:cb17sc), all cells were implanted into mice 1:1 with Matrigel (BD Biosciences). M3 cells (stably infected with MSCV-Luciferase-PGK-Hygro retrovirus) were orthotopically transplanted into the sciatic nerve pocket of mice, and resulting tumors were verified (histopathology by C.R. Antonescu) and regrafted into new mice for DAC studies when tumors reached steady state growth. M14 cells (stably infected with MSCV-Luciferase-PGK-Neo-IRES-GFP retrovirus) were orthotopically transplanted into the sciatic nerve pocket of mice. The resulting tumors were verified (histopathology by C.R. Antonescu), and tumorigenic cell lines were established. These cells were then reinjected into mice for DAC studies when tumors reached steady-state growth. MPNST PDX-1 tumors in CB-17 SCID mice (Taconic, RRID:IMSR_TAC:cb17sc) were enzymatically dissociated, followed by subcutaneous injection into flanks of new CB-17 SCID mice (Taconic, RRID:IMSR_TAC:cb17sc). When tumors reached 50 to 100 mm^3 on average, mice were separated into vehicle (PBS) and DAC treatment groups based on a similar representation of tumor sizes and mouse weights. Mice were treated with vehicle (PBS) or 5 mg/kg DAC (as previously described; ref. 74) by intraperitoneal injection once daily for 3 consecutive days followed by no further treatment for at least 11 days. As previously described (19), 45 mg/kg GSK3685032 or vehicle was formulated and administered by intraperitoneal injection twice daily to mice. M3 and M14 xenograft tumor growth was measured by luciferase bioluminescence imaging as previously described (73). Tumor volume was calculated with the following formula $[(4/3)\pi \times (\text{length}/2) \times (\text{width}/2) \times (\text{depth}/2)]$ using caliper-based measurements of each tumor. For inducible *DNMT1* knockdown xenograft studies, M14 tumorigenic cells (Luciferase$^+$) were stably infected with doxycycline-inducible shRNAs (without doxycycline addition) and orthotopically transplanted into the sciatic nerve pocket of CB-17 SCID mice (Taconic, RRID:IMSR_TAC:cb17sc). For *in vivo* knockdown, mice were fed doxycycline water (200 mg/L + 0.5% sucrose). Xenograft tumor growth was measured by luciferase bioluminescence imaging as previously described (73). All data were plotted with GraphPad (Prism, RRID:SCR_002798).

FACS Analysis

All flow cytometry was performed using LSRFortessa Flow Cytometer (BD Biosciences). GFP-linked shRNA competition assays were performed as described previously (75). Apoptosis was assayed using APC-Annexin V (Tonbo Biosciences) or Annexin V-FITC Kit (Miltenyi Biotec). All data were processed and analyzed with FCS Express 7 Research Edition (De Novo Software, Inc.; RRID:SCR_016431). All data were plotted with GraphPad (Prism, RRID:SCR_002798).

DNA Cloning

Control (sh*Ren*.713), *DNMT1*, *DNMT3A*, and *DNMT3B* shRNAs were cloned into Tet-ON all-in-one plasmids LT3GEPIR (gift from Johannes Zuber, RRID:Addgene_111177) and LT3REPIR (same as LT3GEPIR except for GFP being substituted with dsRed, MSKCC Gene Editing and Screening Core Facility) as previously described (69). Control and *SUZ12* sgRNA targeting the VEFS functional domain were cloned into pL-CRISPR.EFS.Blast (plasmid was generated by replacing tagRFP in Addgene Plasmid #57819 with blasticidin S deaminase antibiotic selection marker) as previously described (76). Human *SUZ12* cDNA was cloned into pLV-EF1α-IRES-Puro (gift from Tobias Meyer, RRID:Addgene_85132). *MAVS* sgRNA was cloned into LRG2.1_Puro (gift from Christopher Vakoc, RRID:Addgene_125594; ref. 77). Control, RNaseL, and PKR sgRNAs were cloned into lenti-CRISPR v2 (gift from Feng Zhang, RRID:Addgene_52961). *STING* shRNAs were cloned into SGEN lentiviral plasmid (gift from Johannes Zuber, RRID:Addgene_111171) for constitutive expression. See Supplementary Table S5 for shRNA and sgRNA target sequences.

RNA Extraction, Reverse Transcription, and Quantitative PCR (qRT-PCR)

Total RNA was isolated from cell lines via TRIzol reagent (Thermo Fisher Scientific). For tissues, samples were disrupted with TissueRuptor II (Qiagen) in TRIzol reagent, followed by RNA isolation. Total RNA (1 μg) was used for cDNA synthesis with a High-Capacity cDNA Reverse Transcription kit (Thermo Fisher Scientific). cDNA and primers were mixed with PowerUp SYBR green 2X master mix (Thermo Fisher Scientific), followed by mRNA quantification with QuantStudio 6 Flex Real-Time PCR System (Applied Biosystems). *RPL27* was used as the housekeeping gene for *in vitro* cells, whereas human-specific *GAPDH* was used as the housekeeping gene for human xenograft tissue samples. Relative fold change gene expression was calculated by the delta-delta Ct method. All data were plotted with GraphPad (Prism, RRID:SCR_002798). See Supplementary Table S6 for qPCR primers used.

Western Blot

Cells were lysed with RIPA buffer (Thermo Fisher Scientific) supplemented with protease and phosphatase inhibitors (Millipore Sigma), followed by brief sonication (Diagenode Bioruptor), and quantified by BCA assay (Thermo Fisher Scientific). Whole-cell lysates were mixed with NuPAGE LDS sample buffer (Thermo Fisher Scientific) supplemented with 2-mercaptoethanol, incubated at 95°C for 10 minutes, and loaded onto NuPAGE 4% to 12% Bis-Tris gels (Thermo Fisher Scientific) for SDS-PAGE followed by protein transfer onto 0.2-μm nitrocellulose membranes (Cytiva Life Sciences) by wet electroblotting at 4°C. Membranes were blocked for 1 hour at room temperature with StartingBlock TBS buffer (Thermo Fisher Scientific) and incubated with primary antibody at 4°C overnight with gentle rotation. The next day, membranes were washed thrice with 1× TBS-T and incubated with HRP-conjugated secondary antibody for 2 hours

at room temperature with gentle rotation. Membranes were washed thrice with 1× TBS-T, followed by application of SuperSignal West Pico PLUS chemiluminescent substrate (Thermo Fisher Scientific) or Immobilon Western chemiluminescent HRP substrate (Millipore Sigma) to membranes and chemiluminescence scanning with ImageQuant LAS4000 (GE Healthcare). See Supplementary Table S7 for antibodies used. Resulting data were processed and cropped with GIMP (GNU Image Manipulation Program, RRID:SCR_003182) open-source software.

Targeted Next-Generation Sequencing Assay

MSK-IMPACT (66) was used to evaluate mutations for 341 cancer genes in human MPNST cell lines and tumors.

RNA-seq and Data Analysis

SUZ12 isogenic M3 MPNST cells were treated in triplicate with or without DNMTi (50 nmol/L daily DAC or 4 μmol/L single dose of GSK862) for 4 days, followed by total RNA isolation. Library preparation and sequencing were conducted by the Integrated Genomics Operation (IGO) core facility at MSKCC. After RiboGreen quantification and quality control by Agilent BioAnalyzer, 500 ng of total RNA with RIN values of 8.3 to 10 underwent polyA selection and TruSeq library preparation according to instructions provided by Illumina (TruSeq Stranded mRNA LT Kit, cat. # RS-122-2102), with 8 cycles of PCR. Samples were barcoded and run on a HiSeq 4000 in a PE50 run using the HiSeq 3000/4000 SBS Kit (Illumina). An average of 41 million paired reads was generated per sample. Ribosomal reads represented 2% of the total reads generated and the percentage of mRNA bases averaged 76%.

RNA sequencing reads were 3′ trimmed for base quality 15 and adapter sequences using version 0.4.5 of TrimGalore (https://www.bioinformatics.babraham.ac.uk/projects/trim_galore, RRID:SCR_011847), and then aligned to human genome assembly hg19 with STAR v2.6 (RRID:SCR_004463) using default parameters. Data quality and transcript coverage were assessed using the Picard tool CollectRNASeqMetrics (http://broadinstitute.github.io/picard/, RRID:SCR_006525).

Transcripts per million (TPM) data were generated via TPMCalculator (78) using default parameters. TPM data for C1, C4, and C6 genes were plotted on violin plots using GraphPad (Prism, RRID:SCR_002798). Read count tables were generated with HTSeq v0.9.1 (RRID:SCR_005514). Normalization and expression dynamics were evaluated with DESeq2 (RRID:SCR_000154) using library size factor normalization, and outliers were assessed by sample grouping in PCA. These library size factors were also used with deepTools v3.1 (RRID:SCR_016366) to create normalized bigwigs using bamCoverage with –scaleFactor.

All differentially expressed genes (FDR <0.1 and $\log_2$ fold change >1.5) from pairwise analyses were then merged to create a union of all contrasts, and *k*-means clustering was performed from $k = 4$ to the point at which cluster groups became redundant. Pathway enrichment (gene sets and GO) was performed on each cluster using Homer v4.5 (http://homer.ucsd.edu, RRID:SCR_010881) and comparing with the cumulative hypergeometric distribution.

For differential expression analysis of REs, we extracted LTRs, SINEs, and LINEs from the repetitive elements annotated by the RepeatMasker (RRID:SCR_012954) and used featureCounts (v1.5.0-p1, RRID:SCR_012919; ref. 79) to count RNA-seq fragments mapped to them. Note that RNA-seq reads mapped to multiple regions were kept by STAR (RRID:SCR_004463). REs with a minimal 10 reads in the RNA-seq samples were retained for differential expression analysis using DESeq2 (RRID:SCR_000154) with default parameters (v1.33.4). Significantly differentially expressed REs (adjusted $P < 0.1$ and fold change >1.5) in at least one of our six comparisons were subject to *k*-means clustering via pheatmap (v.1.0.12, RRID:SCR_016418), separately for the three classes of REs.

Bisulfite-seq and Data Analysis

SUZ12 isogenic M3 MPNST cells were treated with or without DNMTi (50 nmol/L daily DAC or 4 μmol/L single dose of GSK862) for 4 days followed by genomic DNA isolation with the Gentra Puregene cell kit (Qiagen). Bisulfite-seq was conducted by the IGO core facility at MSKCC. Briefly, after PicoGreen quantification and quality control by the Agilent BioAnalyzer, 500 ng of genomic DNA was sheared using an LE220-plus Focused-ultrasonicator (Covaris, cat. #500569). Sequencing libraries were prepared using the KAPA Hyper Prep Kit (Kapa Biosystems KK8504) without PCR amplification. Postligation cleanup proceeded according to Illumina's instructions with 110 μL Sample Purification Mix from the TruSeq Methyl Capture EPIC LT Library Prep Kit (Illumina, cat. #FC-151-1002). After purification, four samples were pooled equivolume and methylome regions were captured using EPIC oligos. Capture pools were bisulfite converted and amplified with 11 cycles of PCR. Pools were sequenced on a HiSeq 2500 in Rapid mode in a 100-bp/100-bp paired-end run using the HiSeq Rapid SBS Kit v2 (Illumina). The average number of read pairs per sample was 61 million. Adapter trimming, alignment to hg19, and CpG methylation calling were done as previously described (80). The *methylKit* (RRID:SCR_005177; ref. 81) R package was used to filter all samples for CpGs with 10 to 400× coverage, followed by tiling the genome into 1,000-bp windows (regions) with 1,000-bp step size, and identification DMRs (≥ ± 25% change). DMRs were annotated via the *annotatr* (82) R package. For intergenic DMRs, the nearest gene was identified by the *closest* function in BEDTools suite (RRID:SCR_006646; ref. 83). Genomation (84) R package (RRID:SCR_003435) was used to annotate CpGs and tiles (regions) with their location (CpG island, shores, promoters) and then plotted as violin plots via ggplot2 (RRID:SCR_014601; ref. 85) package in R. PCA of methylation data at all tiles (regions) was generated in Partek Genomics Suite (v 7.0, RRID:SCR_011860). For DNA methylation profile plots, four individual replicates (PBS rep1 and 2, DMSO rep1 and 2) were averaged for each cell line followed by visualization of the mean DNA methylation profile over regions of interest via plotProfile command from deepTools (RRID:SCR_016366; ref. 86). CGI locations were obtained from the UCSC genome table browser and used for extracting promoter CGIs for subsequent visualization of CpG DNA methylation as density plots or quantification by plotHeatmap and multiBigwigSummary commands, respectively, from deepTools (RRID:SCR_016366; ref. 86).

ChIP-seq and Data Analysis

The recipe for ChIP-related buffers can be found in Supplementary Table S8. *SUZ12*-isogenic M3 MPNST cells were treated with or without DNMTi (50 nmol/L daily DAC or 4 μmol/L single dose of GSK862) for 5 days. Cells were harvested followed by cross-linking with 1% formaldehyde for 10 minutes at room temperature, and were quenched with glycine (125 mmol/L final). Cells were washed twice with sterile cold PBS followed by lysis with LB1 buffer (+protease and phosphatase inhibitors for 10 minutes at 4°C while rotating, pelleted, and resuspended in LB2 buffer (+protease and phosphatase inhibitors) for 10 minutes at 4°C while rotating, and pelleted/resuspended in SLB buffer (+protease and phosphatase inhibitors) for 10 minutes at 4°C while rotating. Lysates were diluted 10-fold with ChIP dilution buffer (+protease and phosphatase inhibitors) followed by chromatin shearing with a Covaris E220 Focused-Ultrasonicator (20% duty cycle + 150W PIP + 200 cycles/burst). Sheared chromatin was centrifuged for 10 minutes at 4°C, and the supernatant was collected followed by the addition of antibody + magnetic protein A/G beads for overnight rotation at 4°C. See Supplementary Table S7 for antibodies used. The next day, beads were washed on a magnetic stand thrice with cold High Salt Wash buffer and once with Low Salt Wash

buffer. Immunoprecipitated chromatin DNA was isolated from beads with elution buffer at 65°C for 30 minutes. Cross-links were reversed overnight at 65°C. ChIP DNA was diluted 2-fold with ChIP TE+NaCl buffer and incubated 2 hours at 37°C with RNaseA, followed by incubation at 55°C for 2 hours with Proteinase K. ChIP DNA was purified by the PCR purification kit (Qiagen). Samples were submitted to the IGO core facility at MSKCC for library construction and sequencing. Briefly, pooled multiplexed libraries were sequenced on a HiSeq 2500 machine in rapid mode at 50-bp paired-end reads per sample.

Adapter sequences were removed from the resulting data with TrimGalore (RRID:SCR_011847) followed by alignment to human genome assembly hg19 using bowtie2 (v2.3.5, RRID:SCR_016368) with default parameters (71). Duplicate reads were removed. Coverage bigwig files were created via bamCoverage command from deepTools (RRID:SCR_016366; ref. 86) to normalize to total reads and human genome size, and subsequent ChIP-seq profiles were visualized either by Integrative Genomics Viewer (87) software or by using the plotHeatmap command from deepTools (RRID:SCR_016366; ref. 86). Genomic regions enriched with H3K27me3 reads were identified using a sliding window method, using input as controls as described previously (88, 89). Genes with peaks in their promoter regions (+/2 kb from TSS) were designated as H3K27em3+ genes.

Statistical Analysis

All experiments (excluding high-throughput sequencing) were repeated at least twice independently, and representative data are shown in the figures. Unless otherwise stated in figure legends, all error bars are shown as the mean ± SEM, and a two-tailed unpaired Student *t* test was used to evaluate statistical significance (*, $P \leq 0.05$; **, $P \leq 0.01$; ***, $P \leq 0.001$; ****, $P \leq 0.0001$). Experimenters were not blind to group assignment and outcome assessment. For drug treatment experiments in animals, mice were assigned to different experimental groups to ensure that the distribution of tumor sizes and mouse weights was similar between groups before starting the treatment.

Data Availability

RNA-seq, bisulfite-seq, and ChIP-seq data have been deposited at the Gene Expression Omnibus (GEO) under accession codes GSE179585, GSE179582, and GSE179586. Any additional information required to reanalyze the data reported in this article is available from the lead contact upon request.

Authors' Disclosures

A.J. Patel reports grants from the NCI during the conduct of the study. M.A. Miranda-Román reports grants from the Department of Defense during the conduct of the study. M.B. Pappalardi reports other support from GSK outside the submitted work. M.T. McCabe reports other support from GSK outside the submitted work. C.M. Rudin reports personal fees from AbbVie, Amgen, AstraZeneca, Bristol Myers Squibb, D2G Oncology, Daiichi Sankyo, Genentech/Roche, Ipsen, Jazz, Kowa, Merck, Syros, Bridge Medicines, Earli, and Harpoon Therapeutics outside the submitted work. S. Chandarlapaty reports grants from Daiichi Sankyo and AmbryX, grants and personal fees from AstraZeneca and Paige.ai, personal fees from Sanofi, Ultivue, and Inivata, and personal fees and nonfinancial support from Novartis outside the submitted work. J.M. Scandura reports other support from AbbVie, Constellation Pharma, CTI Biopharma, and SDP Oncology outside the submitted work, as well as grant support from the NIH, the Cancer Research & Treatment Fund, the Starr Cancer Research Foundation, the MPN Research Foundation, and MPN Peoria. Y. Chen reports other support from Oric Pharmaceuticals and grants from Foghorn outside the submitted work. P. Chi reports grants from the NIH/NCI, the Neurofibromatosis Therapeutic Acceleration Program (NTAP), the Department of Defense, Cycle for Survival Linn Family Discovery Fund, and the Geoffrey Beene Cancer Research Fund during the conduct of the study, as well as personal fees from Deciphera, grants and nonfinancial support from Deciphera, Pfizer/Array, and Ningbo NewBay, and personal fees from Zai Lab and Novartis outside the submitted work. No disclosures were reported by the other authors.

Authors' Contributions

A.J. Patel: Conceptualization, data curation, software, formal analysis, funding acquisition, validation, investigation, visualization, writing–original draft, project administration, writing–review and editing. **S. Warda:** Resources, validation, investigation, writing–review and editing. **J.L. Maag:** Data curation, software, formal analysis, investigation, writing–review and editing. **R. Misra:** Data curation, software, formal analysis, investigation, visualization, writing–review and editing. **M.A. Miranda-Román:** Data curation, formal analysis, validation, investigation, writing–review and editing. **M.R. Pachai:** Resources, investigation, writing–review and editing. **C.J. Lee:** Resources, investigation, methodology, writing–review and editing. **D. Li:** Investigation, writing–review and editing. **N. Wang:** Validation, writing–review and editing. **G. Bayshtok:** Validation, investigation, writing–review and editing. **E. Fishinevich:** Resources, investigation, writing–review and editing. **Y. Meng:** Investigation, writing–review and editing. **E.W.P. Wong:** Methodology, writing–review and editing. **J. Yan:** Resources, methodology, writing–review and editing. **E. Giff:** Investigation, writing–review and editing. **M.B. Pappalardi:** Resources, writing–review and editing. **M.T. McCabe:** Resources, writing–review and editing. **J.A. Fletcher:** Resources, writing–review and editing. **C.M. Rudin:** Resources, writing–review and editing. **S. Chandarlapaty:** Resources, writing–review and editing. **J.M. Scandura:** Methodology, writing–review and editing. **R.P. Koche:** Data curation, software, formal analysis, visualization, writing–review and editing. **J.L. Glass:** Data curation, software, formal analysis, visualization, writing–review and editing. **C.R. Antonescu:** Formal analysis, writing–review and editing. **D. Zheng:** Data curation, software, formal analysis, investigation, visualization, writing–review and editing. **Y. Chen:** Conceptualization, resources, software, supervision, funding acquisition, visualization, project administration, writing–review and editing. **P. Chi:** Conceptualization, resources, supervision, funding acquisition, visualization, writing–original draft, project administration, writing–review and editing.

Acknowledgments

We thank William L. Gerald and Xiaoliang L. Xu (MSKCC) for patient-derived M1, M3, M4, and M6 MPNST cell lines. We thank Jonathan A. Fletcher for patient-derived M14 (ST88-14) and M10 (MPNST1) cell lines, as well as Melissa Pappalardi and Michael McCabe (GSK plc.) for providing GSK862 and GSK3685032, and advice on their usage. We thank Scott Armstrong for generously providing *Eed*$^{f/f}$ mice (67, 68) and Samuel F. Bakhoum for the lentiviral *STING* shRNA plasmid. We thank Makhzuna Khudoynazarova for help with generating the MPNST mouse models and human MPNST CDX model. We thank the laboratory of Alex Kentsis and Charles L. Sawyers for providing cell lines. The IGO core conducted library preparation and next-generation sequencing for ChIP-seq, bisulfite-seq, and RNA-seq samples. Processing and analysis of bisulfite-seq and RNA-seq data were done by the Center for Epigenetics Research (MSKCC). This work was supported in part by grants from the NIH/NCI (R01 CA228216 and DP2 CA174499), Department of Defense (W81XWH-15-1-0124 and W81XWH-22-1-0326), Francis Collins Scholar NTAP, and Cycle for Survival and Linn Family Discovery Fund to P. Chi; an NIH/NCI grant (P50 CA217694) to P. Chi and C.R. Antonescu; NIH/NCI grants (5R01CA208100-04, 5U54CA224079-03, 5P50CA092629-20) to Y. Chen; the Geoffrey Beene Cancer Research

Fund to P. Chi; a Department of Defense Horizon Award (CA181474) to M.A. Miranda-Román; Translational Oncology Research in Oncology Training Program T32 grant (5T32CA160001-09) from the NIH/NCI to A.J. Patel; and an NIH grant (P30 CA008748) to MSKCC (Core Grant). The IGO core was funded by the NCI Cancer Center Support Grant (P30 CA08748), Cycle for Survival, and the Marie-Josée and Henry R. Kravis Center for Molecular Oncology.

The costs of publication of this article were defrayed in part by the payment of page charges. This article must therefore be hereby marked *advertisement* in accordance with 18 U.S.C. Section 1734 solely to indicate this fact.

Note

Supplementary data for this article are available at Cancer Discovery Online (http://cancerdiscovery.aacrjournals.org/).

Received December 20, 2021; revised May 19, 2022; accepted June 29, 2022; published first July 5, 2022.

REFERENCES

1. Margueron R, Reinberg D. The polycomb complex PRC2 and its mark in life. Nature 2011;469:343–9.
2. Varambally S, Dhanasekaran SM, Zhou M, Barrette TR, Kumar-Sinha C, Sanda MG, et al. The polycomb group protein EZH2 is involved in progression of prostate cancer. Nature 2002;419:624–9.
3. Simon JA, Lange CA. Roles of the EZH2 histone methyltransferase in cancer epigenetics. Mutat Res 2008;647:21–9.
4. Morin RD, Johnson NA, Severson TM, Mungall AJ, An J, Goya R, et al. Somatic mutations altering EZH2 (Tyr641) in follicular and diffuse large B-cell lymphomas of germinal-center origin. Nat Genet 2010;42:181–5.
5. Ernst T, Chase AJ, Score J, Hidalgo-Curtis CE, Bryant C, Jones AV, et al. Inactivating mutations of the histone methyltransferase gene EZH2 in myeloid disorders. Nat Genet 2010;42:722–6.
6. Nikoloski G, Langemeijer SM, Kuiper RP, Knops R, Massop M, Tonnissen ER, et al. Somatic mutations of the histone methyltransferase gene EZH2 in myelodysplastic syndromes. Nat Genet 2010;42:665–7.
7. Ntziachristos P, Tsirigos A, Van Vlierberghe P, Nedjic J, Trimarchi T, Flaherty MS, et al. Genetic inactivation of the polycomb repressive complex 2 in T cell acute lymphoblastic leukemia. Nat Med 2012;18:298–301.
8. Zhang J, Ding L, Holmfeldt L, Wu G, Heatley SL, Payne-Turner D, et al. The genetic basis of early T-cell precursor acute lymphoblastic leukaemia. Nature 2012;481:157–63.
9. De Raedt T, Beert E, Pasmant E, Luscan A, Brems H, Ortonne N, et al. PRC2 loss amplifies Ras-driven transcription and confers sensitivity to BRD4-based therapies. Nature 2014;514:247–51.
10. Lee W, Teckie S, Wiesner T, Ran L, Prieto Granada CN, Lin M, et al. PRC2 is recurrently inactivated through EED or SUZ12 loss in malignant peripheral nerve sheath tumors. Nat Genet 2014;46:1227–32.
11. Zhang M, Wang Y, Jones S, Sausen M, McMahon K, Sharma R, et al. Somatic mutations of SUZ12 in malignant peripheral nerve sheath tumors. Nat Genet 2014;46:1170.
12. Lewis PW, Muller MM, Koletsky MS, Cordero F, Lin S, Banaszynski LA, et al. Inhibition of PRC2 activity by a gain-of-function H3 mutation found in pediatric glioblastoma. Science 2013;340:857–61.
13. Schaefer I-M, Fletcher CDM, Hornick JL. Loss of H3K27 trimethylation distinguishes malignant peripheral nerve sheath tumors from histologic mimics. Mod Pathol 2016;29:4–13.
14. Prieto-Granada CN, Wiesner T, Messina JL, Jungbluth AA, Chi P, Antonescu CR. Loss of H3K27me3 expression is a highly sensitive marker for sporadic and radiation-induced MPNST. Am J Surg Pathol 2016;40:479–89.
15. Won HH, Scott SN, Brannon AR, Shah RH, Berger MF. Detecting somatic genetic alterations in tumor specimens by exon capture and massively parallel sequencing. J Vis Exp 2013;(80):e50710.
16. Diaz AA, Qin H, Ramalho-Santos M, Song JS. HiTSelect: a comprehensive tool for high-complexity-pooled screen analysis. Nucleic Acids Res 2015;43:e16.
17. Lyko F. The DNA methyltransferase family: a versatile toolkit for epigenetic regulation. Nat Rev Genet 2017;19:81.
18. Derissen EJB, Beijnen JH, Schellens JHM. Concise drug review: azacitidine and decitabine. Oncologist 2013;18:619–24.
19. Pappalardi MB, Keenan K, Cockerill M, Kellner WA, Stowell A, Sherk C, et al. Discovery of a first-in-class reversible DNMT1-selective inhibitor with improved tolerability and efficacy in acute myeloid leukemia. Nat Cancer 2021;2:1002–17.
20. Knutson SK, Kawano S, Minoshima Y, Warholic NM, Huang K-C, Xiao Y, et al. Selective inhibition of EZH2 by EPZ-6438 leads to potent antitumor activity in EZH2-mutant non-Hodgkin lymphoma. Mol Cancer Ther 2014;13:842–54.
21. Qi W, Zhao K, Gu J, Huang Y, Wang Y, Zhang H, et al. An allosteric PRC2 inhibitor targeting the H3K27me3 binding pocket of EED. Nat Chem Biol 2017;13:381.
22. Deaton AM, Bird A. CpG islands and the regulation of transcription. Genes Dev 2011;25:1010–22.
23. Højfeldt JW, Laugesen A, Willumsen BM, Damhofer H, Hedehus L, Tvardovskiy A, et al. Accurate H3K27 methylation can be established de novo by SUZ12-directed PRC2. Nat Struct Mol Biol 2018;25:225–32.
24. Chiappinelli Katherine B, Strissel Pamela L, Desrichard A, Li H, Henke C, Akman B, et al. Inhibiting DNA methylation causes an interferon response in Cancer via dsRNA including endogenous retroviruses. Cell 2015;162:974–86.
25. Roulois D, Loo Yau H, Singhania R, Wang Y, Danesh A, Shen Shu Y, et al. DNA-demethylating agents target colorectal cancer cells by inducing viral mimicry by endogenous transcripts. Cell 2015;162:961–73.
26. Bartok E, Hartmann G. Immune sensing mechanisms that discriminate self from altered self and foreign nucleic acids. Immunity 2020;53:54–77.
27. Hur S. Double-stranded RNA sensors and modulators in innate immunity. Annu Rev Immunol 2019;37:349–75.
28. Mehdipour P, Marhon SA, Ettayebi I, Chakravarthy A, Hosseini A, Wang Y, et al. Epigenetic therapy induces transcription of inverted SINEs and ADAR1 dependency. Nature 2020;588:169–73.
29. Payer LM, Burns KH. Transposable elements in human genetic disease. Nat Rev Genet 2019;20:760–72.
30. Roers A, Hiller B, Hornung V. Recognition of endogenous nucleic acids by the innate immune system. Immunity 2016;44:739–54.
31. Schlee M, Hartmann G. Discriminating self from non-self in nucleic acid sensing. Nat Rev Immunol 2016;16:566–80.
32. Lanciano S, Cristofari G. Measuring and interpreting transposable element expression. Nat Rev Genet 2020;21:721–36.
33. Cowan LA, Talwar S, Yang AS. Will DNA methylation inhibitors work in solid tumors? a review of the clinical experience with azacitidine and decitabine in solid tumors. Epigenomics 2010;2:71–86.
34. Jin N, George TL, Otterson GA, Verschraegen C, Wen H, Carbone D, et al. Advances in epigenetic therapeutics with focus on solid tumors. Clinical Epigenetics 2021;13:83.
35. Lima-Junior DS, Krishnamurthy SR, Bouladoux N, Collins N, Han SJ, Chen EY, et al. Endogenous retroviruses promote homeostatic and inflammatory responses to the microbiota. Cell 2021;184:3794–811.
36. Tan X, Sun L, Chen J, Chen ZJ. Detection of microbial infections through innate immune sensing of nucleic acids. Annu Rev Microbiol 2018;72:447–78.
37. Lugrin J, Martinon F. The AIM2 inflammasome: Sensor of pathogens and cellular perturbations. Immunol Rev 2018;281:99–114.
38. Chung H, Calis JJA, Wu X, Sun T, Yu Y, Sarbanes SL, et al. Human ADAR1 prevents endogenous RNA from triggering translational shutdown. Cell 2018;172:811–24.e14.
39. Clavarino G, Cláudio N, Couderc T, Dalet A, Judith D, Camosseto V, et al. Induction of GADD34 is necessary for dsRNA-dependent interferon-β production and participates in the control of chikungunya virus infection. PLoS Pathog 2012;8:e1002708.

40. Italiano A, Soria JC, Toulmonde M, Michot JM, Lucchesi C, Varga A, et al. Tazemetostat, an EZH2 inhibitor, in relapsed or refractory B-cell non-Hodgkin lymphoma and advanced solid tumours: a first-in-human, open-label, phase 1 study. Lancet Oncol 2018;19:649–59.
41. Morschhauser F, Tilly H, Chaidos A, McKay P, Phillips T, Assouline S, et al. Tazemetostat for patients with relapsed or refractory follicular lymphoma: an open-label, single-arm, multicentre, phase 2 trial. Lancet Oncol 2020;21:1433–42.
42. Min B, Park JS, Jeong YS, Jeon K, Kang YK. Dnmt1 binds and represses genomic retroelements via DNA methylation in mouse early embryos. Nucleic Acids Res 2020;48:8431–44.
43. Ha K, Lee GE, Palii SS, Brown KD, Takeda Y, Liu K, et al. Rapid and transient recruitment of DNMT1 to DNA double-strand breaks is mediated by its interaction with multiple components of the DNA damage response machinery. Hum Mol Genet 2011;20:126–40.
44. Robertson KD, Uzvolgyi E, Liang G, Talmadge C, Sumegi J, Gonzales FA, et al. The human DNA methyltransferases (DNMTs) 1, 3a and 3b: coordinate mRNA expression in normal tissues and overexpression in tumors. Nucleic Acids Res 1999;27:2291–8.
45. Verma N, Pan H, Doré LC, Shukla A, Li QV, Pelham-Webb B, et al. TET proteins safeguard bivalent promoters from de novo methylation in human embryonic stem cells. Nat Genet 2018;50:83–95.
46. Linnekamp JF, Butter R, Spijker R, Medema JP, van Laarhoven HWM. Clinical and biological effects of demethylating agents on solid tumours – a systematic review. Cancer Treat Rev 2017;54:10–23.
47. Qiu T, Zhou L, Zhu W, Wang T, Wang J, Shu Y, et al. Effects of treatment with histone deacetylase inhibitors in solid tumors: a review based on 30 clinical trials. Future Oncol 2013;9:255–69.
48. Richon VM. Cancer biology: mechanism of antitumour action of vorinostat (suberoylanilide hydroxamic acid), a novel histone deacetylase inhibitor. Br J Cancer 2006;95:S2–S6.
49. Schrump DS, Fischette MR, Nguyen DM, Zhao M, Li X, Kunst TF, et al. Phase I study of decitabine-mediated gene expression in patients with cancers involving the lungs, esophagus, or pleura. Clin Cancer Res 2006;12:5777–85.
50. Banerjee S, Gusho E, Gaughan C, Dong B, Gu X, Holvey-Bates E, et al. OAS-RNase L innate immune pathway mediates the cytotoxicity of a DNA-demethylating drug. Proc Natl Acad Sci 2019;116:5071–6.
51. Bou-Nader C, Gordon JM, Henderson FE, Zhang J. The search for a PKR code—differential regulation of protein kinase R activity by diverse RNA and protein regulators. RNA 2019;25:539–56.
52. Chau V, Lim SK, Mo W, Liu C, Patel AJ, McKay RM, et al. Preclinical therapeutic efficacy of a novel pharmacologic inducer of apoptosis in malignant peripheral nerve sheath tumors. Cancer Res 2014;74:586–97.
53. Cichowski K, Shih TS, Schmitt E, Santiago S, Reilly K, McLaughlin ME, et al. Mouse models of tumor development in neurofibromatosis type 1. Science 1999;286:2172–6.
54. Johannessen CM, Johnson BW, Williams Sybil MG, Chan AW, Reczek EE, Lynch RC, et al. TORC1 is essential for NF1-associated malignancies. Curr Biol 2008;18:56–62.
55. Johansson G, Mahller YY, Collins MH, Kim MO, Nobukuni T, Perentesis J, et al. Effective in vivo targeting of the mammalian target of rapamycin pathway in malignant peripheral nerve sheath tumors. Mol Cancer Ther 2008;7:1237–45.
56. Lock R, Ingraham R, Maertens O, Miller AL, Weledji N, Legius E, et al. Cotargeting MNK and MEK kinases induces the regression of NF1-mutant cancers. J Clin Invest 2016;126:2181–90.
57. Mo W, Chen J, Patel A, Zhang L, Chau V, Li Y, et al. CXCR4/CXCL12 mediate autocrine cell-cycle progression in NF1-associated malignant peripheral nerve sheath tumors. Cell 2013;152:1077–90.
58. Patel Amish J, Liao CP, Chen Z, Liu C, Wang Y, Le Lu Q. BET bromodomain inhibition triggers apoptosis of NF1-associated malignant peripheral nerve sheath tumors through bim induction. Cell Rep 2014;6:81–92.
59. Vogel KS, Klesse LJ, Velasco-Miguel S, Meyers K, Rushing EJ, Parada LF. Mouse tumor model for neurofibromatosis type 1. Science 1999;286:2176–9.
60. Watson AL, Keller BJ, Williams KA, Damle NN, Finnerty SJ, Anderson LK, et al. Co-targeting the MAPK and PI3K/AKT/mTOR pathways in two genetically engineered mouse models of schwann cell tumors reduces tumor grade and multiplicity. Oncotarget 2014;5:1502–14.
61. Watson AL, Rahrmann EP, Moriarity BS, Choi K, Conboy CB, Greeley AD, et al. Canonical Wnt/beta-catenin signaling drives human Schwann cell transformation, progression, and tumor maintenance. Cancer Discov 2013;3:674–89.
62. Wu J, Patmore DM, Jousma E, Eaves DW, Breving K, Patel AV, et al. EGFR–STAT3 signaling promotes formation of malignant peripheral nerve sheath tumors. Oncogene 2014;33:173–80.
63. Dhillon S. Decitabine/cedazuridine: first approval. Drugs 2020;80:1373–8.
64. Duchmann M, Itzykson R. Clinical update on hypomethylating agents. Int J Hematol 2019;110:161–9.
65. Nervi C, De Marinis E, Codacci-Pisanelli G. Epigenetic treatment of solid tumours: a review of clinical trials. Clin Epigenetics 2015;7:127.
66. Cheng DT, Mitchell TN, Zehir A, Shah RH, Benayed R, Syed A, et al. Memorial Sloan Kettering-Integrated Mutation Profiling of Actionable Cancer Targets (MSK-IMPACT): a hybridization capture-based next-generation sequencing clinical assay for solid tumor molecular oncology. J Mol Diagn 2015;17:251–64.
67. Neff T, Sinha AU, Kluk MJ, Zhu N, Khattab MH, Stein L, et al. Polycomb repressive complex 2 is required for MLL-AF9 leukemia. Proc Natl Acad Sci 2012;109:5028–33.
68. Xie H, Xu J, Hsu Jessie H, Nguyen M, Fujiwara Y, Peng C, et al. Polycomb repressive complex 2 regulates normal hematopoietic stem cell function in a developmental-stage-specific manner. Cell Stem Cell 2014;14:68–80.
69. Fellmann C, Hoffmann T, Sridhar V, Hopfgartner B, Muhar M, Roth M, et al. An optimized microRNA backbone for effective single-copy RNAi. Cell Rep 2013;5:1704–13.
70. Martin M. Cutadapt removes adapter sequences from high-throughput sequencing reads. EMBnet J 2011;17:3.
71. Langmead B, Salzberg SL. Fast gapped-read alignment with Bowtie 2. Nat Methods 2012;9:357–9.
72. Robinson MD, McCarthy DJ, Smyth GK. edgeR: a Bioconductor package for differential expression analysis of digital gene expression data. Bioinformatics 2009;26:139–40.
73. Cooper JM, Patel AJ, Chen Z, Liao C-P, Chen K, Mo J, et al. Overcoming BET inhibitor resistance in malignant peripheral nerve sheath tumors. Clin Cancer Res 2019;25:3404–16.
74. Yu J, Qin B, Moyer AM, Nowsheen S, Liu T, Qin S, et al. DNA methyltransferase expression in triple-negative breast cancer predicts sensitivity to decitabine. J Clin Invest 2018;128:2376–88.
75. Ran L, Chen Y, Sher J, Wong EWP, Murphy D, Zhang JQ, et al. FOXF1 defines the core-regulatory circuitry in gastrointestinal stromal tumor. Cancer Discov 2018;8:234–51.
76. Heckl D, Kowalczyk MS, Yudovich D, Belizaire R, Puram RV, McConkey ME, et al. Generation of mouse models of myeloid malignancy with combinatorial genetic lesions using CRISPR-Cas9 genome editing. Nat Biotechnol 2014;32:941–6.
77. Tarumoto Y, Lin S, Wang J, Milazzo JP, Xu Y, Lu B, et al. Salt-inducible kinase inhibition suppresses acute myeloid leukemia progression in vivo. Blood 2020;135:56–70.
78. Vera Alvarez R, Pongor LS, Mariño-Ramírez L, Landsman D. TPMCalculator: one-step software to quantify mRNA abundance of genomic features. Bioinformatics 2018;35:1960–2.
79. Liao Y, Smyth GK, Shi W. featureCounts: an efficient general purpose program for assigning sequence reads to genomic features. Bioinformatics 2013;30:923–30.
80. Glass JL, Hassane D, Wouters BJ, Kunimoto H, Avellino R, Garrett-Bakelman FE, et al. Epigenetic identity in AML depends on disruption of nonpromoter regulatory elements and is affected by antagonistic effects of mutations in epigenetic modifiers. Cancer Discov 2017;7:868–83.
81. Akalin A, Kormaksson M, Li S, Garrett-Bakelman FE, Figueroa ME, Melnick A, et al. methylKit: a comprehensive R package for the analysis of genome-wide DNA methylation profiles. Genome Biol 2012;13:R87.
82. Cavalcante RG, Sartor MA. annotatr: genomic regions in context. Bioinformatics 2017;33:2381–3.

83. Quinlan AR, Hall IM. BEDTools: a flexible suite of utilities for comparing genomic features. Bioinformatics 2010;26:841–2.
84. Akalin A, Franke V, Vlahovicek K, Mason CE, Schubeler D. Genomation: a toolkit to summarize, annotate and visualize genomic intervals. Bioinformatics 2015;31:1127–9.
85. Wickham H. ggplot2: Elegant graphics for data analysis: use R! Cham (Switzerland): Springer International Publishing; 2016.
86. Ramírez F, Dündar F, Diehl S, Grüning BA, Manke T. deepTools: a flexible platform for exploring deep-sequencing data. Nucleic Acids Res 2014;42:W187–W91.
87. Robinson JT, Thorvaldsdóttir H, Winckler W, Guttman M, Lander ES, Getz G, et al. Integrative genomics viewer. Nat Biotechnol 2011;29:24–6.
88. Cohen I, Bar C, Liu H, Valdes VJ, Zhao D, Galbo PM, et al. Polycomb complexes redundantly maintain epidermal stem cell identity during development. Genes Dev 2021;35:354–66.
89. Li J, Galbo PM, Gong W, Storey AJ, Tsai YH, Yu X, et al. ZMYND11-MBTD1 induces leukemogenesis through hijacking NuA4/TIP60 acetyltransferase complex and a PWWP-mediated chromatin association mechanism. Nat Commun 2021;12:1045.